COMENIUS UNIVERSITY IN BRATISLAVA
FACULTY OF MATHEMATICS, PHYSICS AND INFORMATICS

DYNAMICS OF DEFORMABLE POROUS MATERIALS

MASTER'S THESIS

2017 Bc. Martin KRÁTKY

COMENIUS UNIVERSITY IN BRATISLAVA
FACULTY OF MATHEMATICS, PHYSICS AND INFORMATICS

DYNAMICS OF DEFORMABLE POROUS MATERIALS

MASTER'S THESIS

Study programme:	Mathematical Economics, Finance and Modelling
Field of study:	1114 Applied Mathematics
Department:	Department of Applied Mathematics and Statistics
Supervisor:	doc. RNDr. Peter Guba, PhD.

Bratislava 2017 **Bc. Martin KRÁTKY**

Comenius University in Bratislava
Faculty of Mathematics, Physics and Informatics

THESIS ASSIGNMENT

Name and Surname:	Bc. Martin Krátky
Study programme:	Mathematical Economics, Finance and Modelling (Single degree study, master II. deg., full time form)
Field of Study:	Applied Mathematics
Type of Thesis:	Diploma Thesis
Language of Thesis:	English
Secondary language:	Slovak

Title: Dynamics of deformable porous materials.

Aim: The thesis is focused on the study of Newtonian flows in deformable porous media.
The aim is to obtain and interpret the numerical solutions that include the effects of gravity, capillarity and background solid-fraction distribution.

Supervisor:	doc. RNDr. Peter Guba, PhD.
Department:	FMFI.KAMŠ - Department of Applied Mathematics and Statistics
Head of department:	prof. RNDr. Daniel Ševčovič, DrSc.

Assigned: 21.01.2016

Approved: 25.01.2016 prof. RNDr. Daniel Ševčovič, DrSc.
Guarantor of Study Programme

.....
Student

.....
Supervisor

Acknowledgements I would like to express my sincere gratitude to my supervisor doc. RNDr. Peter Guba, PhD. for his guidance, insightful comments and patience.

Abstrakt v štátnom jazyku

KRÁTKY, Martin: Dynamika deformovateľných pórovitých materiálov [Diplomová práca], Univerzita Komenského v Bratislave, Fakulta matematiky, fyziky a informatiky, Katedra aplikovanej matematiky a štatistiky; školiteľ: doc. RNDr. Peter Guba, PhD., Bratislava, 2017, 58 s.

V práci skúmame dynamiku kapilárneho nasiakavania kvapaliny do deformovateľného pórovitého materiálu. Uvažujeme jednorozmerný prípad, kedy kvapalina samovoľne infiltruje do homogénneho pórovitého materiálu vplyvom kapilárnych síl, ktoré sú orientované v opačnom smere ako gravitácia. Model je založený na teórii zmesí, v ktorej je každý objemový element ponímaný ako dokonalá zmes pevnej a kvapalnej fázy. V jednorozmernom prípade sa problém redukuje na parciálnu diferenciálnu rovnicu s dvoma voľnými hranicami, ktoré sú riadené dvojicou obyčajných diferenciálnych rovníc. Predchádzajúca analýza problému (Siddique et al., 2009) sa zaoberala prípadom lineárnej funkcie napätia pevnej fázy a lineárnej lomenej funkcie pre permeabilitu pórovitého prostredia. V našej práci analyzujeme prípady nelineárnych funkcií napätia a permeability, ktoré sú konzistentné s existujúcimi experimentálnymi meraniami (Sommer and Mortensen, 1996). Numerické riešenie modelu je založené na metóde čiar s využitím pseudospektrálnej a konečno diferenčnej diskretizácie priestorovej premennej. Identifikujeme 3 kvalitatívne odlišné módy dynamiky pevnej fázy: permanentná kompresia, počiatočná kompresia a následná relaxácia a permanentná relaxácia pórovitého materiálu. Získané riešenia porovnávame s experimentom (Siddique et al., 2009). Výsledky práce nájdu aplikáciu v kontexte fázovej premeny viaczložkových zmesí.

Kľúčové slová: Deformovateľný pórovitý materiál, Nasiakavanie, Kapilárny tlak, Pseudospektrálna metóda

Abstract

KRÁTKY, Martin: Dynamics of deformable porous materials [Master's Thesis], Comenius University in Bratislava, Faculty of Mathematics, Physics and Informatics, Department of Applied Mathematics and Statistics; Supervisor: doc. RNDr. Peter Guba, PhD., Bratislava, 2017, 58 p.

We investigate the capillary imbibition of a liquid into a deformable porous material. We consider a one-dimensional case when the liquid infiltrates into a homogenous porous material due to capillary forces oriented in a direction opposite to the gravity force. The mathematical model is based on mixture theory, which considers each volume element as a perfect mixture of the solid and liquid phases. The one-dimensional reduction results in a free boundary problem with boundary positions being governed by two ordinary differential equations. Previous analysis of the problem (Siddique et al., 2009) considered a linear stress function and a linear rational permeability function. Our work analyzes the effects of nonlinear stress and permeability functions that are consistent with existing experimental measurements (Sommer and Mortensen, 1996). Numerical implementation employs the method of lines using pseudospectral and finite difference discretizations of the spatial variable. We identify three qualitatively different modes of solid phase behavior: permanent shrinkage; initial shrinkage and final relaxation and permanent relaxation of the porous material. We compare the results with existing experiment (Siddique et al., 2009). The results find application in studying phase changes of multiphase systems.

Keywords: Deformable Porous Material, Imbibition, Capillary Pressure, Pseudospectral Method

Contents

Introduction

Modeling fluid flow in porous materials is a problem interesting from both the theoretical and practical perspective. One encounters such problems in various engineering and scientific fields such as groundwater flow, oil recovery, studying phase changes or flows in biological tissues. On microscopic level, classical approaches from fluid dynamics can be used considering single pores and the microscopic structure of the material. On a larger scale; however, it becomes infeasible to both describe the geometry of the problem in detail and to numerically model the flow. Mixture theory overcomes such difficulties by averaging the material properties over each volume element. Considering each volume element as a continuum consisting of the liquid and solid phase simultaneously allows us to apply approaches from continuum mechanics. Henry Darcy's pioneering experiments concerning the flow of water through beds of sand related the fluid velocity to the pressure gradient and sand permeability [6]. It was later shown that this relation can be obtained from the microscopic level approach by the method of averaging [11].

If one allows the solid material to deform, the problems become even more interesting. In such situations, the fluid flow deforms the porous material, which affects the material porosity and thus it's resistance to flow. Such problems arise in areas including oil recovery, textile engineering or flows in biological tissues. The constituents in our model undergo no phase changes, i.e. no mass transfer between the phases occurs. Situations involving phase changes are discussed in [4].

In section 1, we derive the general model using mixture theory framework by applying mass and momentum balances, following [5]. We proceed to a one-dimensional reduction of the governing equations, which results in a free boundary problem. We consider a setup similar to those in [7], [9], i.e. the liquid spontaneously infiltrates into the porous material due to capillary forces acting in a direction opposite to the gravity force. Our main contribution is that we propose a physically realistic class of stress and permeability functions motivated by experimental measurements in [10].

In section 2, we present a further reduction, namely the zero-gravity case. Using similarity transformation, the problem is transformed into a boundary value problem with unknown parameters. We employ a numerical scheme based on pseudospectral and

finite difference spatial discretizations. The resulting system of nonlinear equations is solved in MATLAB using nested *fsolve* routines. We analyze the effect of the stress and permeability functions on the solutions as well as the effect of the remaining parameters in the model.

In section 3, equations governing the steady state are derived. We make an assumption that a steady state exists, which is later justified by numerical simulations. Again, the effects of stress and permeability functions as well as the remaining parameters are analyzed.

Section 4 focuses on the general time-dependent problem with present gravity field. The resulting nonlinear free boundary problem involving a PDE for the solid volume fraction $\phi(z,t)$ with 2 ODEs governing the boundary positions is solved using the method of lines. Again, pseudospectral and finite difference methods are used for discretization of the spatial variable. The early-time dynamics follows the zero-gravity case from section 2 and the system reaches a steady state described in section 3. We compare our results for various configurations of stress and permeability functions with the experiments in [9]. In dependence on material parameters representing the capillary pressure and the solid volume fraction of the unsaturated porous material, we identify three qualitatively different modes of the solid phase evolution.

1 Mathematical model

We start by deriving the equations governing fluid imbibition and solid deformation [5]. These equations will be based on so-called mixture theory framework, which considers each volume element to be a continuum consisting of several (perfectly blended) phases. In this thesis, we will be considering two phases – solid (porous material) and liquid; however, the number of phases can be arbitrary. The final equations will be transformed into dimensionless form. To distinguish between the dimensional and dimensionless quantities, the dimensional will be marked with an asterisk.

We assume that each infinitesimal elementary volume δV^* (representing a point in space) contains enough material of both phases that the solid and liquid volumes δV_s^* and δV_l^* contained in δV^* can be defined. One of the quantities of interest will be the solid volume fraction ϕ defined as

$$\phi = \frac{\delta V_s^*}{\delta V^*} \in [0, 1],$$

for each elementary volume δV^*. Since $\delta V^* = \delta V_s^* + \delta V_l^*$, liquid volume fraction equals $1 - \phi$ and we will not define this quantity separately. If we denote the masses of each phase contained in the elementary volume as δm_s^* and δm_l^*, the local densities of each phase can be defined

$$\rho_s^* = \frac{\delta m_s^*}{\delta V^*}, \qquad \rho_l^* = \frac{\delta m_l^*}{\delta V^*}.$$

The local density of the mixture is then defined as

$$\rho_m^* = \frac{\delta m^*}{\delta V^*} = \frac{\delta m_s^* + \delta m_l^*}{\delta V^*} = \rho_s^* + \rho_l^*.$$

The last needed quantities will be the local speed of the solid and liquid phases $\boldsymbol{v}_s^*$ and $\boldsymbol{v}_l^*$ respectively.

We arrived at local quantities defined in each point of space, representing averaged properties of the mixture in each infinitesimally small elementary volume, regardless of their macroscopic structure. This lets us apply the approaches from continuum mechanics based on principles of mass and momentum conservation. Since we assume no phase changes and therefore no mass transport between the solid and liquid phase, the mass conservation equations will be independent. The coupling of the equations occurs in the momentum equations, since mutual forces acting between the phases are

assumed. Situations involving phase changes and mass transfer between the solid and liquid phases are discussed in [4].

1.1 Mass and momentum conservation

Let us consider an arbitrary finite control volume V^* with smooth boundary ∂V^* and outward pointing unit normal $\hat{\boldsymbol{n}}^*$. The change of liquid mass contained in V^* should be equal to the mass of the influx/outflux through the boundary, i.e.

$$\frac{\mathrm{d}}{\mathrm{d}t^*}\int\limits_{V^*}\rho_s^* dV^* + \int\limits_{\partial V^*}\rho_s^*(\boldsymbol{v}_s^*\cdot\hat{\boldsymbol{n}}^*)dA^* = 0. \tag{1.1}$$

The same applies to the solid phase

$$\frac{\mathrm{d}}{\mathrm{d}t^*}\int\limits_{V^*}\rho_l^* dV^* + \int\limits_{\partial V^*}\rho_l^*(\boldsymbol{v}_l^*\cdot\hat{\boldsymbol{n}}^*)dA^* = 0. \tag{1.2}$$

By applying the divergence theorem, equations 1.1 and 1.2 can be transformed into differential form

$$\frac{\partial\rho_s^*}{\partial t^*} + \nabla^*\cdot(\rho_s^*\boldsymbol{v}_s^*) = 0, \tag{1.3}$$

$$\frac{\partial\rho_l^*}{\partial t^*} + \nabla^*\cdot(\rho_l^*\boldsymbol{v}_l^*) = 0. \tag{1.4}$$

In each finite control volume, momentum must be conserved, which is enforced by the following equations

$$\frac{\mathrm{d}}{\mathrm{d}t^*}\int\limits_{V^*}\rho_s^*\boldsymbol{v}_s^* dV^* + \int\limits_{\partial V^*}\rho_s^*\boldsymbol{v}_s^*(\boldsymbol{v}_s^*\cdot\hat{\boldsymbol{n}}^*)dA^* = \int\limits_{V^*}(\rho_s^*\boldsymbol{g}^* + \boldsymbol{\pi}_s^*)dV^* + \int\limits_{\partial V^*}(\mathbf{T}_s^*\cdot\hat{\boldsymbol{n}}^*)dA^*, \tag{1.5}$$

$$\frac{\mathrm{d}}{\mathrm{d}t^*}\int\limits_{V^*}\rho_l^*\boldsymbol{v}_l^* dV^* + \int\limits_{\partial V^*}\rho_l^*\boldsymbol{v}_l^*(\boldsymbol{v}_l^*\cdot\hat{\boldsymbol{n}}^*)dA^* = \int\limits_{V^*}(\rho_l^*\boldsymbol{g}^* + \boldsymbol{\pi}_l^*)dV^* + \int\limits_{\partial V^*}(\mathbf{T}_l^*\cdot\hat{\boldsymbol{n}}^*)dA^*. \tag{1.6}$$

The right-hand side represents the total change of momentum in the control volume, where the first term accounts for the change of momentum inside the control volume. The second term accounts for the change of momentum due to mass influx/outflux. This change of momentum is caused by forces acting on the control volume, represented by the right-hand side fo equations (1.5), (1.6). Here $\boldsymbol{g}^*$ is the gravity acceleration, $\boldsymbol{\pi}_s^*$ and $\boldsymbol{\pi}_l^*$ are the momentum transfers due to friction forces acting between the phases. Note that from Newton's second law $\boldsymbol{\pi}_s^* = -\boldsymbol{\pi}_l^*$, which couples the equations (1.5)

and (1.6). $\boldsymbol{T}_s^*$ and $\boldsymbol{T}_l^*$ are the stress tensors of the solid and liquid phase respectively. These stress tensors take into account the presence of both phases and are different from those when only one phase is considered. Following [5], both stress tensors can be decomposed into their normal (given by pressure field p^*) and tangential components

$$\boldsymbol{T}_s^* = -\phi p^* \mathbf{I} + \boldsymbol{\sigma}_s^*, \tag{1.7}$$

$$\boldsymbol{T}_l^* = -(1-\phi) p^* \mathbf{I} + \boldsymbol{\sigma}_l^*. \tag{1.8}$$

More on defining and measuring stress tensors in mixtures can be found in [7]. We will skip this discussion and return to it in the one-dimensional model where stress tensors take form of scalar functions.

Applying the divergence theorem results in the differential form of equations (1.5) and (1.6)

$$\rho_s^* \left(\frac{\partial \boldsymbol{v}_s^*}{\partial t^*} + (\boldsymbol{v}_s^* \cdot \nabla) \boldsymbol{v}_s^* \right) = \nabla^* \cdot \mathbf{T}_s^* + \rho_s^* \boldsymbol{g}^* + \boldsymbol{\pi}_s^*, \tag{1.9}$$

$$\rho_l^* \left(\frac{\partial \boldsymbol{v}_l^*}{\partial t^*} + (\boldsymbol{v}_l^* \cdot \nabla) \boldsymbol{v}_l^* \right) = \nabla^* \cdot \mathbf{T}_l^* + \rho_l^* \boldsymbol{g}^* + \boldsymbol{\pi}_l^*. \tag{1.10}$$

Adding these two equations together, using the mutually opposite friction forces $\boldsymbol{\pi}_s^* = -\boldsymbol{\pi}_l^*$ and defining mixture velocity $\rho_m^* \boldsymbol{v}_m^* = \rho_s^* \boldsymbol{v}_s^* + \rho_l^* \boldsymbol{v}_l^*$, after some manipulation, momentum balance for the mixture can be obtained

$$\rho_m^* \left(\frac{\partial \boldsymbol{v}_m^*}{\partial t^*} + (\boldsymbol{v}_m^* \cdot \nabla^*) \boldsymbol{v}_m^* \right) = \nabla^* \cdot \mathbf{T}_m^* + \rho_m^* \boldsymbol{g}^*, \tag{1.11}$$

where $\mathbf{T}_m^*$ is the stress tensor of the mixture in the form

$$\mathbf{T}_m^* = -p^* \mathbf{I} + \boldsymbol{\sigma}_s^* + \boldsymbol{\sigma}_l^* - \rho_s^* (\boldsymbol{v}_s^* - \boldsymbol{v}_m^*) \otimes (\boldsymbol{v}_s^* - \boldsymbol{v}_m^*) - \rho_l^* (\boldsymbol{v}_l^* - \boldsymbol{v}_m^*) \otimes (\boldsymbol{v}_l^* - \boldsymbol{v}_m^*). \tag{1.12}$$

Here, $\otimes$ is the vector outer product, in a more mathematical way for a column vector $\boldsymbol{v}$ given by $\boldsymbol{v}\boldsymbol{v}^T$. Following [2], we set the friction force terms to be

$$\boldsymbol{\pi}_l^* = -\boldsymbol{\pi}_s^* = \frac{\mu^* (1-\phi)^2}{k^*(\phi)} (\boldsymbol{v}_l^* - \boldsymbol{v}_s^*) - p^* \nabla^* \phi, \tag{1.13}$$

where μ^* is the fluid viscosity and $k^*(\phi)$ the permeability of the porous material as a function of the solid volume fraction ϕ.

1.1.1 Resulting model

Since the actual solid and liquid velocities are to be of small magnitude, velocity gradients contained in the left-hand sides of equations (1.9)–(1.11) as well as the tangential component of liquid stress $\boldsymbol{\sigma}_l^*$ in (1.8) can be neglected [5], [6]. Furthermore, we replace the spatially dependent solid and liquid densities ρ_s^*, ρ_l^* with constant true densities of the respective phases ρ_s^{*T}, ρ_l^{*T}. As a result, we obtain the equation representing the hydrostatic balance of liquid phase

$$0 = \nabla^* \cdot \big(-(1-\phi)p^*\mathbf{I}\big) + \rho_l^{*T}\boldsymbol{g}^* + \frac{\mu^*(1-\phi)^2}{k^*(\phi)}\big(\boldsymbol{v}_s^* - \boldsymbol{v}_l^*\big) - p^*\nabla^*\phi \tag{1.14}$$

and balance of the mixture

$$0 = \nabla^* \cdot \big(-p^*\mathbf{I} + \sigma_s^*\big) + \rho_m^*\boldsymbol{g}^*. \tag{1.15}$$

After rearrangement, we arrive at the final system of equations governing fluid flow and solid deformation

$$\boldsymbol{v}_l^* - \boldsymbol{v}_s^* = \frac{k^*(\phi)}{\mu^*(1-\phi)}\big[-\nabla^* p^* + \rho_l^T \boldsymbol{g}^*\big], \tag{1.16}$$

$$0 = -\nabla^* p^* + \nabla^* \cdot \boldsymbol{\sigma}_s^* + \rho_m^*\boldsymbol{g}^*, \tag{1.17}$$

$$0 = \frac{\partial \phi}{\partial t^*} + \nabla^* \cdot (\phi \boldsymbol{v}_s^*), \tag{1.18}$$

$$0 = \frac{\partial \phi}{\partial t^*} - \nabla^* \cdot ((1-\phi)\boldsymbol{v}_l^*). \tag{1.19}$$

Note, that the first two equations are vector equations while the other two are scalar. The unknown variables are the solid and fluid velocities $\boldsymbol{v}_s^*$, $\boldsymbol{v}_l^*$, pressure field p^* and the field representing spatially-dependent solid volume fraction ϕ. We leave the specification of $\boldsymbol{\sigma}_s^*$ together with $k^*(\phi)$ to the one dimensional case, where they attain the form of scalar functions.

1.2 One-dimensional reduction

This thesis focuses on the one-dimensional reduction of the equations (1.16)–(1.19) with single spatial variable z^* oriented parallel to the direction of gravity acceleration $\boldsymbol{g}^*$. We consider a deformable porous material fixed at its upper side. The material is homogenous and its dimension in the xy plane are large enough, so that the flow is also

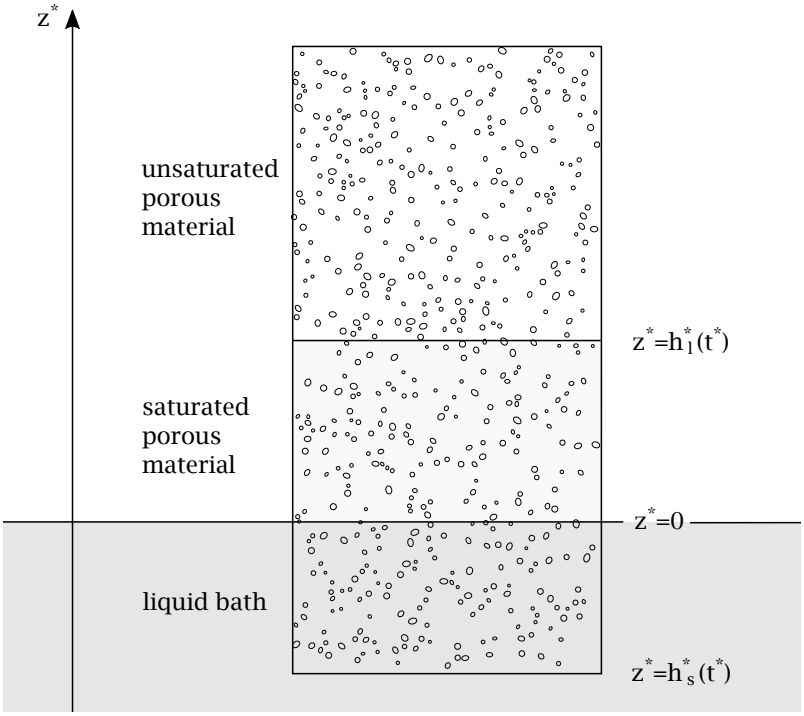

Figure 1: $h_s^* = h_s^*(t^*)$ - time-dependent position of the interface between liquid and saturated solid (solid front), $h_l^* = h_l^*(t^*)$ - time-dependent position of the interface between unsaturated and saturated solid (liquid front), $z^* = 0$ - surface of the liquid bath.

homogenous and we can restrict our attention to a single spatial variable z^*. At $t^* = 0$, the lower side of the porous material gets into contact with the surface of the liquid at $z^* = 0$. The liquid then spontaneously starts to infiltrate into the porous material due to capillary suction. The presence of liquid in the porous material releases its inner stress and the material relaxes, resulting (in most cases) in submerging of the lower parts of the porous material. This solid deformation changes the volume fraction of the saturated solid affecting its permeability to the fluid flow. Imbibition thus changes mechanical properties of the porous material, which in turn change the dynamics of the imbibition. To avoid movement of the fluid surface (i.e. movement of the origin $z^* = 0$) due to part of the fluid being imbibed into the material, we assume the fluid bath to be infinite. We will denote the interface between liquid and the saturated porous material $h_s^*(t^*)$ (solid front) and the interface between the unsaturated and saturated porous material $h_l^*(t^*)$ (liquid front), as shown in the schematic figure 1. At $t^* = 0$, $h_s^* = h_l^* = 0$.

The whole system is subject to atmospheric pressure p_A^*. At the solid interface

$h_s^*(t^*)$, we assume hydrostatic pressure together with the so-called zero stress condition

$$p^*(h_s^*, t^*) = p_A^* - {\rho_l^*}^T g^* h_s^*, \qquad \sigma^*(h_s^*, t^*) = 0. \tag{1.20}$$

Note that due to only the gradient of the stress function appearing in equations (1.16)–(1.19), we could set the stress to be arbitrary number. The important fact is that we assume the stress to be constant at the solid interface and zero was chosen for simplicity. At the liquid interface, atmospheric and constant capillary (which actually drives the flow) pressures are present

$$p^*(h_l^*, t^*) = p_A^* + p_c^*. \tag{1.21}$$

1.2.1 Nondimensionalized system

We now introduce dimensionless quantities which will be used throughout the rest of this thesis

$$z = \frac{z^*}{L^*}, \qquad t = \frac{t^*}{T^*}, \qquad p = \frac{p^*}{\Sigma_0^*}, \qquad k(\phi) = \frac{k^*(\phi)}{K_0^*}, \qquad \sigma(\phi) = \frac{\sigma^*(\phi)}{\Sigma_0^*}, \tag{1.22}$$

where Σ_0^* is a representative stress scale and K_0^* a representative permeability scale. The representative length and time scales are then given by $L^* = \Sigma_0^*/{\rho_l^*}^T g^*$, $T^* = {L^*}^2 \mu^*/K_0^* \Sigma_0^*$. As a corollary, the remaining quantities are nondimensionalized accordingly

$$v_s = \frac{v_s^*}{L^*/T^*}, \qquad v_l = \frac{v_l^*}{L^*/T^*}, \qquad h_s = \frac{h_s^*}{L^*}, \qquad h_l = \frac{h_l^*}{L^*}. \tag{1.23}$$

By nondimensionalizing the one-dimensional equivalent of equations (1.16)-(1.19), we arrive at the system

$$\frac{\partial \phi}{\partial t} + \frac{\partial}{\partial z}(\phi v_s) = 0, \tag{1.24}$$

$$\frac{\partial \phi}{\partial t} - \frac{\partial}{\partial z}((1-\phi) v_l) = 0, \tag{1.25}$$

$$v_l - v_s = -\frac{k(\phi)}{(1-\phi)}\left(\frac{\partial p}{\partial z} + 1\right), \tag{1.26}$$

$$0 = -\frac{\partial p}{\partial z} + \frac{\partial \sigma}{\partial z} - (\rho\phi + 1), \tag{1.27}$$

where $\rho = {\rho_s^*}^T/{\rho_l^*}^T - 1$. Note that we have naturally arrived at a generalized form of Darcy's law in equation (1.26). It puts the relative velocity of fluid into relation with the pressure gradient and gravity, that are driving the flow. The relative fluid

velocity is also proportional to the permeability of the material. In the one-dimensional reduction, we naturally expect the permeability to be directly dependent on the solid volume fraction ϕ, which determines how much of the volume is occupied by solid. As we already suggested, the stress function σ is going to be a scalar function also depending on the solid volume fraction $\sigma = \sigma(\phi)$.

If we denote the dimensionless atmospheric pressure $p_A := p_A^*/\Sigma_0^*$ and the dimensionless capillary pressure $p_c := p_c^*/\Sigma_0^*$, the dimensionless form of boundary conditions (1.20) and (1.21) takes form

$$p(h_s, t) = p_A - h_s, \qquad \sigma(h_s, t) = 0. \tag{1.28}$$

$$p(h_l, t) = p_A + p_c. \tag{1.29}$$

Note that the constant atmospheric pressure p_A can be left out.

We now eliminate the pressure field from the equations and obtain a single partial differential equation for solid volume fraction $\phi(z, t)$ together with two ordinary differential equations governing the evolution of solid and liquid front positions.

Subtracting (1.25) from (1.24) and integrating with respect to z gives a term valid for all z

$$-\phi(v_l - v_s) + v_l = c(t), \tag{1.30}$$

where $c(t)$ is a constant of integration allowing for dependence on time t. Plugging this into (1.26) gives us a formula for v_l

$$v_l = c(t) - \phi\frac{k(\phi)}{1-\phi}\left(\frac{\partial p}{\partial z} + 1\right). \tag{1.31}$$

Formula for solid phase velocity can be obtained by plugging (1.31) into (1.30)

$$v_s = c(t) + k(\phi)\left(\frac{\partial p}{\partial z} + 1\right). \tag{1.32}$$

Using the direct dependence of the stress function σ on ϕ and rearranging equation (1.27) yields

$$\frac{\partial p}{\partial z} + 1 = \sigma'(\phi)\frac{\partial \phi}{\partial z} - \rho\phi, \tag{1.33}$$

which can be in turn used in the equations (1.31), (1.32) to eliminate pressure

$$v_l = c(t) - \phi\frac{k(\phi)}{1-\phi}\left(\sigma'(\phi)\frac{\partial \phi}{\partial z} - \rho\phi\right), \tag{1.34}$$

$$v_s = c(t) + k(\phi)\left(\sigma'(\phi)\frac{\partial \phi}{\partial z} - \rho\phi\right). \tag{1.35}$$

Finally, substituting equation (1.34) into equation (1.24) results in a partial differential equation

$$\frac{\partial \phi}{\partial t} + c(t)\frac{\partial \phi}{\partial z} = -\frac{\partial}{\partial z}\left[\phi k(\phi)\left\{\sigma'(\phi)\frac{\partial \phi}{\partial z} - \rho\phi\right\}\right]. \tag{1.36}$$

The equation for $c(t)$ can be derived from the following assumptions, discussed in detail in [1], [7]: $\phi(h_l^+) = \phi_0$, $v_s(h_l^+) = 0$ and $v_l(h_l^+) = v_l(h_l^-)$. ϕ_0 is the solid volume fraction of the unsaturated (rigid) porous material. The second equation tells us, that the porous material right above the liquid front is rigid. The third equation equates the liquid velocities below and above the liquid front. The liquid velocity above the liquid front can be viewed as the vapor velocity. Evaluating equation (1.30) at both sides of the interface h_l and using these assumption gives us a system of equations

$$c(t) = (1 - \phi_0)v_l(h_l^-), \tag{1.37}$$

$$c(t) = \phi(h_l^-)v_s(h_l^-) + (1 - \phi(h_l^-))v_l(h_l^-), \tag{1.38}$$

which by combining yields

$$c(t) = \left(\frac{1 - \phi_0}{\phi - \phi_0}\phi v_s\right)\Bigg|_{h_l^-}. \tag{1.39}$$

However, we do not expect the velocity of the solid *below* the liquid front $v_s(h_l^-)$ to be of simple form, thus we use the equation (1.35) to obtain the final form of the time-dependent constant $c(t)$

$$c(t) = -\frac{(1 - \phi_0)}{\phi_0}\left[\frac{\phi k(\phi)}{(1 - \phi)}\left(\sigma'(\phi)\frac{\partial \phi}{\partial z} - \rho\phi\right)\right]\Bigg|_{h_l^-}. \tag{1.40}$$

Evaluating equation (1.34) at h_l^- and equation (1.35) at h_s^+ yields ordinary differential equations governing the evolution of interface positions

$$v_s(h_s^+) = \frac{\mathrm{d}h_s}{\mathrm{d}_t} = c(t) + k(\phi)\left(\sigma'(\phi)\frac{\partial \phi}{\partial z} - \rho\phi\right)\Bigg|_{h_s^+} \tag{1.41}$$

$$v_l(h_l^-) = \frac{\mathrm{d}h_l}{\mathrm{d}_t} = c(t) + \frac{\phi k(\phi)}{(1 - \phi)}\left(\sigma'(\phi)\frac{\partial \phi}{\partial z} - \rho\phi\right)\Bigg|_{h_l^-}. \tag{1.42}$$

From a practical viewpoint, the actual interface positions can be directly measured and are therefore of greater interest than the overall solid and liquid velocity fields or the solid volume fraction.

1.2.2 Final one-dimensional model

For the sake of clarity, we restate the final set of equations to be solved in the following sections

$$\frac{\partial \phi}{\partial t} + c(t)\frac{\partial \phi}{\partial z} = -\frac{\partial}{\partial z}\left[\phi k(\phi)\left\{\sigma'(\phi)\frac{\partial \phi}{\partial z} - \rho\phi\right\}\right], \tag{1.43}$$

where

$$c(t) = -\frac{(1-\phi_0)}{\phi_0}\left[\frac{\phi k(\phi)}{(1-\phi)}\left(\sigma'(\phi)\frac{\partial \phi}{\partial z} - \rho\phi\right)\right]\Bigg|_{h_l^-}. \tag{1.44}$$

$$\frac{dh_s}{dt} = c(t) + k(\phi)\left(\sigma'(\phi)\frac{\partial \phi}{\partial z} - \rho\phi\right)\Bigg|_{h_s^+}, \tag{1.45}$$

$$\frac{dh_l}{dt} = c(t) + \frac{\phi k(\phi)}{(1-\phi)}\left(\sigma'(\phi)\frac{\partial \phi}{\partial z} - \rho\phi\right)\Bigg|_{h_l^-}. \tag{1.46}$$

Note that the equation (1.43) is a highly nonlinear partial differential equation. It is in fact a free boundary problem with boundaries evolving in time, following the equations (1.45) and (1.46). Furthermore, the coefficient $c(t)$ is also dependent on the interface position h_l. Thus, none of these equations can be solved separately, which poses a challenging and careful numerical implementation.

The initial positions of the interfaces are

$$h_s(t=0) = h_l(t=0) = 0. \tag{1.47}$$

Boundary condition for $\phi(h_s, t)$ is derived from the the dimensionless boundary condition (1.28) using the direct dependence of the stress function on ϕ. We denote this value ϕ_r

$$\phi(h_s, t) = \sigma^{-1}(0) =: \phi_r. \tag{1.48}$$

Boundary condition for $\phi(h_l, t)$ can be obtained by integrating the equation (1.27) from h_s to h_l and applying boundary conditions for pressure

$$\sigma(\phi(h_l, t)) = p_c + h_s + \int_{h_s(t)}^{h_l(t)} (\rho\phi + 1)\mathrm{d}z. \tag{1.49}$$

For an initial profile for $\phi(z, t_0), t_0 \ll 1$, we use self-similar profile derived in section 2 representing zero-gravity case. Since $p(h_l, t) - p(h_s, t)$ is $\mathcal{O}(1)$ for $t \to 0$, $\mathrm{d}p/\mathrm{d}z \to -\infty$ as $t \to 0$. Thus, neglecting constant gravity force for early times is reasonable.

1.3 Stress and permeability functions

For the model to be complete, we need to define physically realistic forms of stress and permeability functions. Since we have focused our attention on the one-dimensional case, these will be scalar functions. The main difference between rigid and deformable porous materials rests in the space-(and time-) dependent solid volume fraction ϕ. Thus, it is natural to model these functions as being directly dependent on ϕ.

We expect the permeability to be a decreasing function of ϕ, i.e. higher fraction of the total volume being occupied by solid results in its higher resistance to the flow and therefore lower permeability. For $\phi = 1$, the permeability should be zero. However, we will not demand our functions to have these global properties. As we shall see, the solid volume fraction varies within a relatively small interval. We will therefore aim to best fit experimental measurements in [10] within the interval of interest.

Note that in the final set of equations (1.43)-(1.46) we are only dealing with the derivative of the stress function. In a similar way to pressure (since we are now in one spatial dimension, so the stress does not have a tangential component), the gradient, rather than the absolute magnitude of stress plays a role. The important message here is that we expect σ to be a decreasing function of ϕ. In other words, for $\phi < \phi_r$, we will be speaking of relative expansion of the porous material and for $\phi > \phi_r$ we will be speaking of relative compression of the porous material.

In [1], [9], the authors study in detail the linear stress function $\sigma^{SAB}(\phi) = \phi_r - \phi$ and permeability function of the form $k^{SAB}(\phi) = \phi_r/\phi$. This choice significantly simplifies the governing equations and leads to a closed-form solution in the case with no gravity.

A more realistic choice of stress and permeability functions based on experimental measurements can be found in [10]. Even though the experimental setup in [10] is slightly different from ours – the liquid is wetting the porous material under external pressure – this is one of a few direct measurements of the dependence of stress on solid volume fraction. The authors then fitted their experimental measurements with the following polynomial of seventh degree (in dimensional terms)

$$\sigma^{*SM}(\phi) = a + b\phi + c\phi^2 + d\phi^3 + e\phi^4 + f\phi^5 + g\phi^6 + h\phi^7, \tag{1.50}$$

with $a = -2.33 \times 10^7$ Pa, $b = 7.13 \times 10^8$ Pa, $c = -9.26 \times 10^9$ Pa, $d = 6.60 \times 10^{10}$ Pa, $e = -2.79 \times 10^{11}$ Pa, $f = 7.02 \times 10^{11}$ Pa, $g = -9.70 \times 10^{11}$ Pa and $h = 5.70 \times 10^{11}$ Pa.

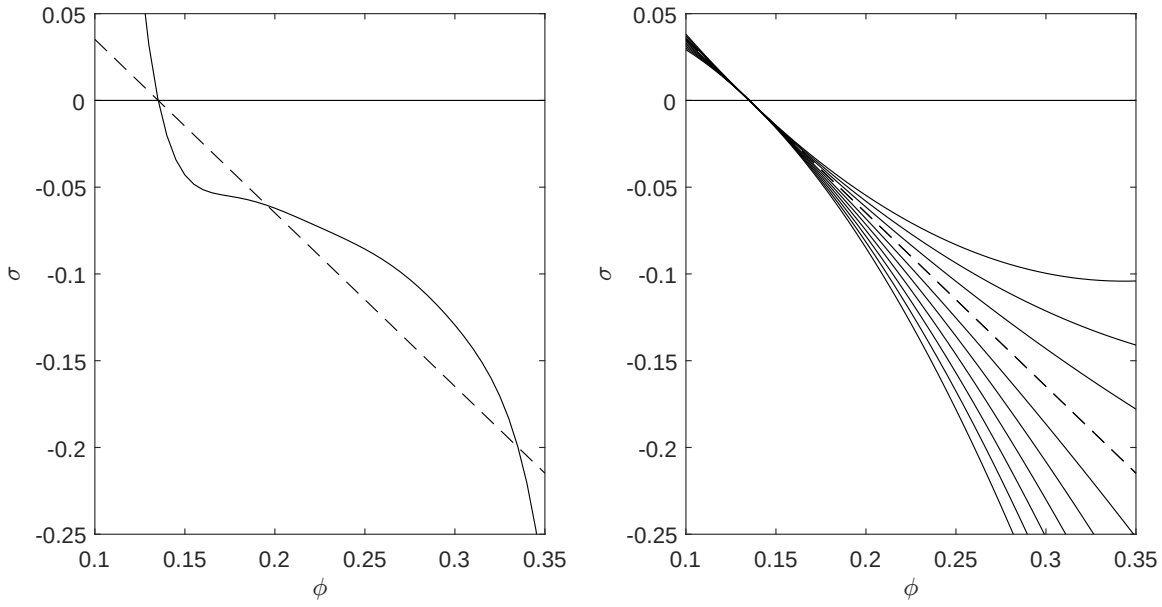

Figure 2: (left) Linear stress function σ^{SAB} and the 7^{th} degree polynomial stress function σ^{SM}. (right) Parametric class of stress functions considered in this thesis.

Figure 2 compares this function to the linear case. Following [5], we nondimensionalized σ^{*SM} with $\Sigma_0^* = 5 \times 10^5$ Pa.

Another experimental measurement in [10] regards the permeability function. The authors fitted their four measurements with an exponentially decreasing function $k^{SM} = 10^{6.9654(\phi_r - \phi)}$. We nondimensionalized this function to have a unit value at ϕ_r. Figure 3 displays the linear rational permeability function k^{SAB}, the exponential permeability function k^{SM} and the four data points.

In this thesis, we would like to focus on a broader class of stress and permeability functions and examine their effect on the solutions. Based on [10] a suitable class for permeability functions seems to be of the form

$$k(\phi) = 10^{\beta(\phi_r - \phi)}, \qquad \beta > 0. \tag{1.51}$$

As we shall see, ϕ effectively varies in a range close to ϕ_r, so we nondimensionalized these functions to obtain a unit value at ϕ_r.

A class of polynomials of 7^{th} degree is too broad. Furthermore, as we already mentioned, ϕ varies from a relatively small range, thus we chose the stress function to be linear with a quadratic correction

$$\sigma(\phi) = (\phi_r - \phi) + \alpha(\phi_r - \phi)^2. \tag{1.52}$$

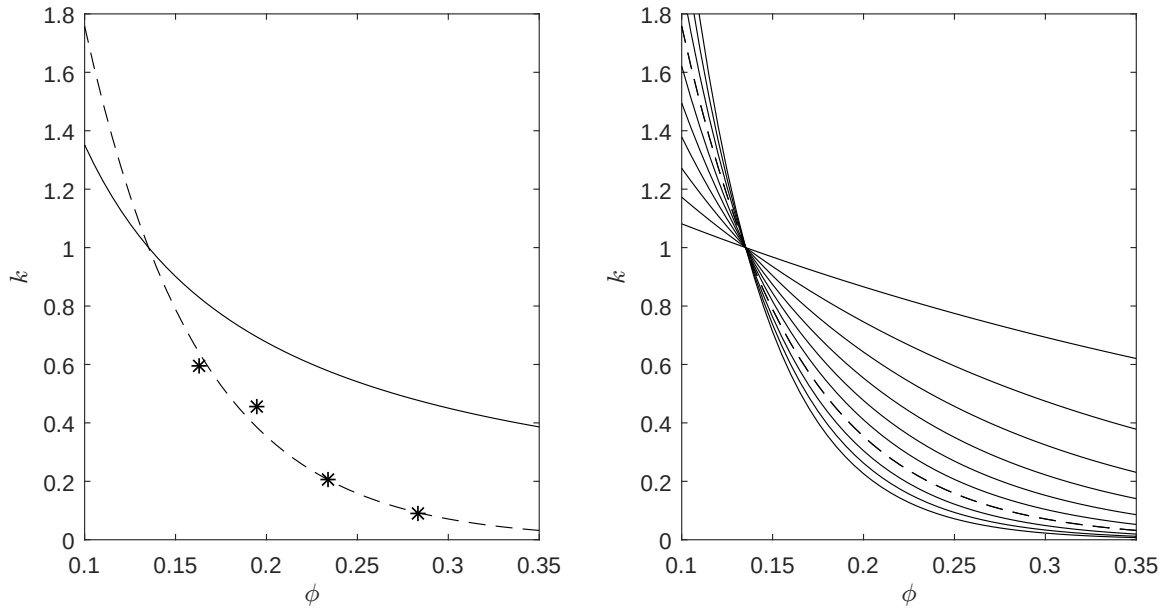

Figure 3: (left) Linear rational permeability function k^{SAB} (solid line) versus exponential permeability function σ^{SM} (dashed line) together with four experimental measurements. (right) Parametric class of permeability functions examined in this thesis.

Both function classes are displayed in the right plots of figures 2 and 3.

2 Zero-gravity

We begin our analysis with a further reduction when there is no gravity acting on the system. Investigating such a problem might seem of little practical importance; however, solutions to this problem are consistent with early-time dynamics of experimental measurements [9]. Furthermore, we will use these solutions as an asymptotic approximation of the initial condition for the general case with gravity field present.

Omitting all terms ivolving $\boldsymbol{g}^*$ in the dimensional set of equations and following the consequent derivation, we arrive at the same equations as in (1.43)-(1.46) only without the terms involving ρ. In equations (1.48), (1.49) the absence of gravity causes no hydrostatic and atmospheric pressure resulting in $p(h_s, t) = 0$, $p(h_l, t) = p_c$. By introducing a similarity transformation, we will be able to transform the partial differential equation (1.43) to an ordinary differential equation.

This differential equation has an analytic solution for simple stress and permeability functions proposed in [9]. With the parametric class of stress and permeability functions (1.51), (1.52) considered in this thesis we will need to rely solely on numerical solution.

The introduction of a similarity variable and following transformation to an ordinary differential equation might seem as a felicitously chosen substitution from a mathematical viewpoint. However, it is a manifestation of thermodynamical laws that determine the form of such a transformation.

2.1 Similarity transformation

We start by introducing a similarity variable $\eta = z/(2\sqrt{t})$. The corresponding differential operators transform to

$$\frac{\partial}{\partial t} = -\frac{\eta}{2t}\frac{\mathrm{d}}{\mathrm{d}\eta}, \qquad \frac{\partial}{\partial z} = \frac{1}{2\sqrt{t}}\frac{\mathrm{d}}{\mathrm{d}\eta}. \tag{2.1}$$

Omitting the terms $\rho\phi$, the equations (1.43)–(1.46) transform to

$$-\eta\frac{1}{2t}\frac{\mathrm{d}\phi}{\mathrm{d}\eta} + c(t)\frac{1}{2\sqrt{t}}\frac{\mathrm{d}\phi}{\mathrm{d}\eta} = -\frac{1}{4t}\frac{\mathrm{d}}{\mathrm{d}\eta}\left[\phi k(\phi)\sigma'(\phi)\frac{\mathrm{d}\phi}{\mathrm{d}\eta}\right], \tag{2.2}$$

$$c(t) = -\frac{1-\phi_0}{\phi_0}\frac{1}{2\sqrt{t}}\left[\frac{\phi k(\phi)}{(1-\phi)}\sigma'(\phi)\frac{\mathrm{d}\phi}{\mathrm{d}\eta}\right]\Bigg|_{\eta=\frac{h_l(t)^-}{2\sqrt{t}}}, \tag{2.3}$$

$$\frac{\mathrm{d}h_s}{\mathrm{d}t} = c(t) + \frac{1}{2\sqrt{t}}\left[k(\phi)\sigma'(\phi)\frac{\mathrm{d}\phi}{\mathrm{d}\eta}\phi\right]\Big|_{\eta=\frac{h_s(t)^+}{2\sqrt{t}}}, \tag{2.4}$$

$$\frac{\mathrm{d}h_l}{\mathrm{d}t} = c(t) + \frac{1}{2\sqrt{t}}\left[\frac{\phi k(\phi)}{(1-\phi)}\sigma'(\phi)\frac{\mathrm{d}\bar{\phi}}{\mathrm{d}\eta}\right]\Big|_{\eta=\frac{h_l(t)^-}{2\sqrt{t}}}. \tag{2.5}$$

If we guessed the form of $h_s(t), h_l(t)$ to be

$$h_s(t) = 2\lambda_s\sqrt{t}, \qquad h_l(t) = 2\lambda_l\sqrt{t}, \tag{2.6}$$

where λ_s, λ_l are unknown constants, the values $\eta = \frac{h_s^+}{2\sqrt{t}}, \eta = \frac{h_l^+}{2\sqrt{t}}$ would become λ_s, λ_l. In other words, η is now from a fixed interval $[\lambda_s, \lambda_l]$. With this choice $c(t)$ becomes

$$c(t) = -\frac{(1-\phi_0)}{\phi_0}\frac{1}{2\sqrt{t}}\left[\frac{\phi k(\phi)}{(1-\phi)}\sigma'(\phi)\frac{\mathrm{d}\phi}{\mathrm{d}\eta}\right]\Big|_{\eta=\lambda_l^-}, \tag{2.7}$$

which does not contradict the $t^{-1/2}$ nature of $\mathrm{d}h_s/\mathrm{d}t$, $\mathrm{d}h_l/\mathrm{d}t$. Furthermore, we are now able to eliminate t from the equation (2.2) and obtain an ordinary differential equation

$$2\eta\frac{\mathrm{d}\phi}{\mathrm{d}\eta} + \frac{1-\phi_0}{\phi_0}\left[\frac{\phi k(\phi)}{(1-\phi)}\sigma'(\phi)\frac{\mathrm{d}\phi}{\mathrm{d}\eta}\right]\Big|_{\lambda_l^-}\frac{\mathrm{d}\phi}{\mathrm{d}\eta} = \frac{\mathrm{d}}{\mathrm{d}\eta}\left[\phi k(\phi)\sigma'(\phi)\frac{\mathrm{d}\phi}{\mathrm{d}\eta}\right]. \tag{2.8}$$

We got a nonlinear boundary value problem with unknown parameters λ_s, λ_l. The values of these parameters can be computed by plugging (2.6) into (2.4), (2.5)

$$\lambda_s = \frac{1}{2}\left(-\frac{1-\phi_0}{\phi_0}\left[\frac{\phi k(\phi)\sigma'(\phi)}{1-\phi}\frac{\mathrm{d}\phi}{\mathrm{d}\eta}\right]\Big|_{\lambda_l^-} + \left[k(\phi)\sigma'(\phi)\frac{\mathrm{d}\phi}{\mathrm{d}\eta}\right]\Big|_{\lambda_s^+}\right), \tag{2.9}$$

$$\lambda_l = -\frac{1}{2\phi_0}\left[\frac{\phi k(\phi)\sigma'(\phi)}{1-\phi}\frac{\mathrm{d}\phi}{\mathrm{d}\eta}\right]\Big|_{\lambda_l^-}. \tag{2.10}$$

To sum up, our task is to solve the boundary value problem (2.8) (the boundary values yet to be specified) on an unknown domain $[\lambda_s, \lambda_l]$ while simultaneously satisfying equations (2.9) and (2.10). A quick analysis suggests that our problem could be well-posed, since we have a second order ODE with 4 equations for 4 constants (boundary conditions together with (2.9) and (2.10)). Section 5 describes in detail the numerical scheme used to solve these equations.

For both boundaries λ_s and λ_l, Dirichlet boundary conditions can be obtained. At $\eta = \lambda_s$ the boundary condition follows from the zero-stress condition (1.28)

$$\phi(h_s, t) = \phi(\lambda_s) = \phi_r. \tag{2.11}$$

The boundary conditions for $\eta = \lambda_l$ can be obtained by integrating the zero-gravity form of equation (1.27) (obtained by omitting the term $\rho\phi + 1$) and using the corresponding boundary conditions for pressure outlined in the beginning of this section. We denote this value ϕ_l.

$$\phi(h_l, t) = \phi(\lambda_l) = \sigma^{-1}(p_c) =: \phi_l. \tag{2.12}$$

For the case of stress function with quadratic correction (1.52), this leads to a simple quadratic equation.

2.2 Solutions

We first illustrate the obtained solutions on three fundamental configurations of stress and permeability functions

1. σ linear, k linear rational (following [9]),
2. σ linear, k exponential (representing classes (1.52) with $\alpha = 0$ and (1.51) with $\beta = 6.9654$),
3. σ 7^{th} degree polynomial, k exponential (following [10]).

These configurations and the numbers assigned to them will be used throughout this thesis.

Figure 4 depicts the corresponding solutions together with the evolution of interface positions. The domain of each profile $\phi(\eta)$ is given by the parameter values $[\lambda_s, \lambda_l]$. These parameters also determine the speed of propagation of the interfaces. All profiles are increasing (given by the boundary conditions). The nonlinear stress function results in highly convex profile for ϕ. The liquid front positions for configurations (2) and (3) are almost identical (they share the same permeability function), the solid deformation for the case of nonlinear stress function is greater.

2.2.1 Parametric class of stress and permeability functions

This section analyzes the effect of varying parameters of the stress and permeability functions on the solutions. The right limit of the range for constant α was chosen so, that the derivative of the stress function is nonzero for $\phi \in [\phi_r, \phi_l]$.

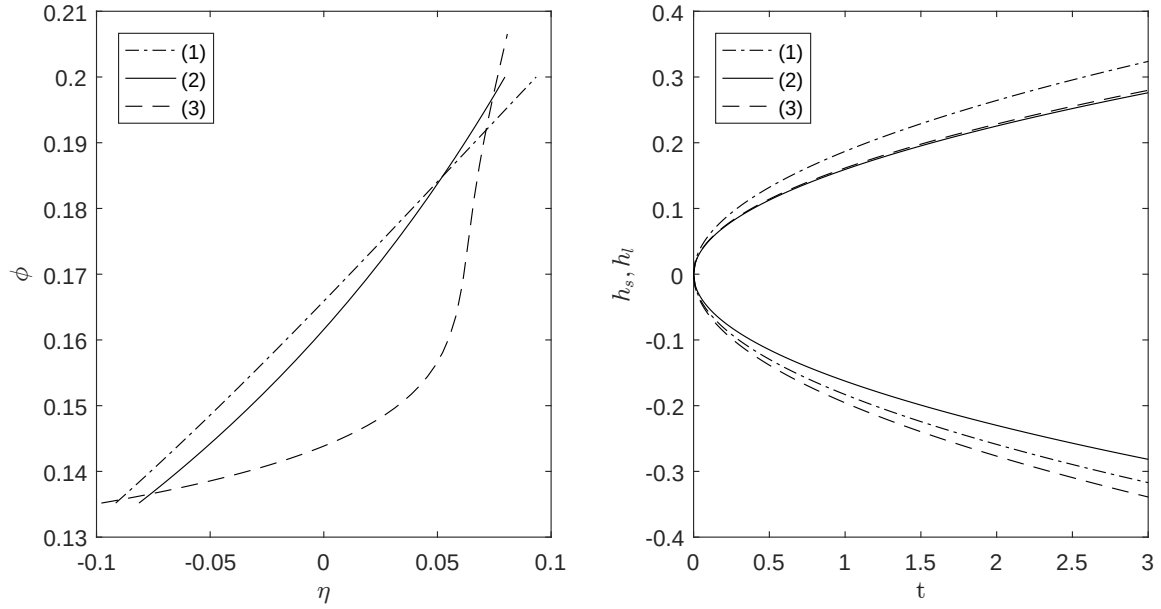

Figure 4: Profiles $\phi(\eta)$ for the three configurations of stress and permeability functions (left) and the evolution of interface positions in time (right). In all configurations $\phi_0 = 0.33$, $\phi_r = 0.135$ and $p_c = -0.065$.

The stress function governing the solid deformation mainly affects the position of the solid front, determined by constant λ_s, while having only minor effect on the liquid front position. The profile $\phi(\eta)$ is mainly determined by the boundary value $\phi_l = \sigma^{-1}(p_c)$ (figure 5). Note that for higher values of α, a boundary layer at λ_l with high gradients of ϕ begins to form.

The permeability function, representing the resistance of the porous material to liquid infiltration, affects the speed of propagation of both interfaces almost equally (figure 6). With increasing β, the absolute values of both λ_s and λ_l decrease. This has a simple reason. Despite the whole class of permeability function having unit value at ϕ_r, with increasing β, the permeability function decays more rapidly and the effective (averaged) permeability is lower. As a result, the liquid propagates slower having also a slower response in the solid deformation.

2.2.2 Effects of the parameters ϕ_0 and p_c

As we shall see, the remaining parameters ϕ_0 and p_c strongly determine the behavior of the system. Note that in the absence of gravity, the solutions do not depend on the

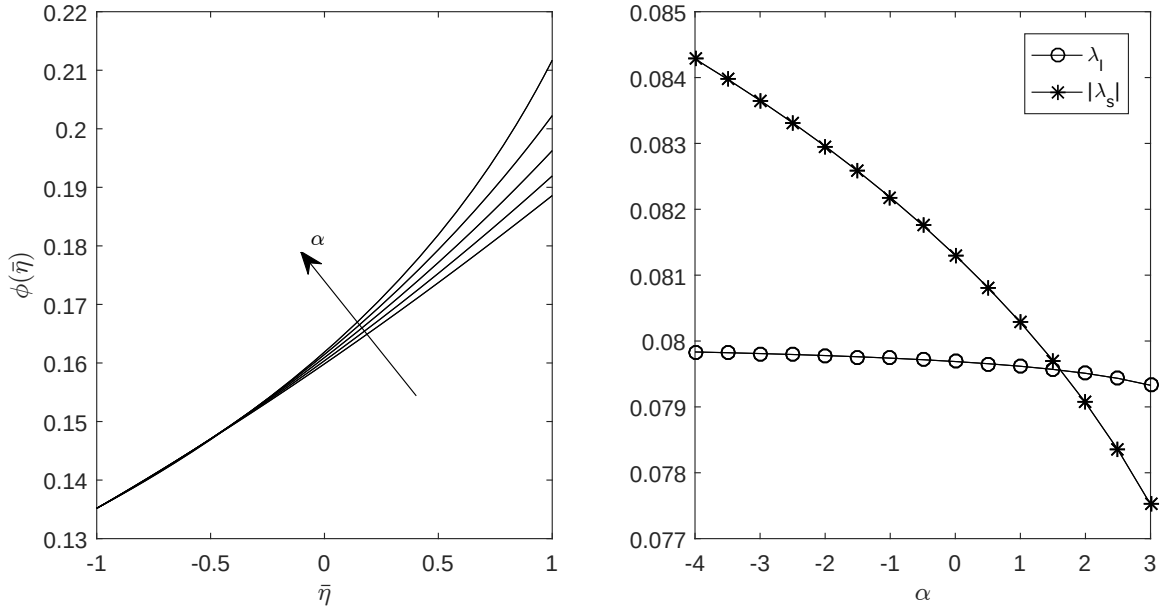

Figure 5: Profiles $\phi(\bar{\eta})$ (η rescaled to $[-1, 1]$) as dependent on the stress function parameter α (left) and the corresponding values of λ_s and λ_l (right). λ_s is displayed in absolute value for better visualization. In all three configurations $\phi_0 = 0.33$, $\phi_r = 0.135$ and $p_c = -0.065$.

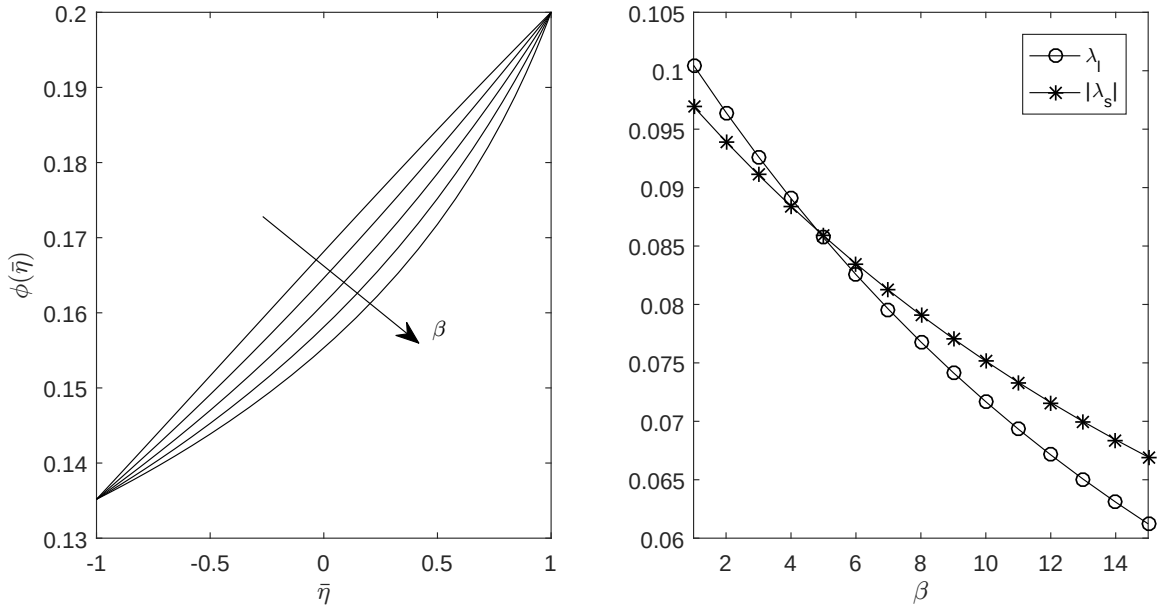

Figure 6: Profiles $\phi(\bar{\eta})$ (η rescaled to $[-1, 1]$) as dependent on the permeability function parameter β (left) and the corresponding values of λ_s and λ_l (right). λ_s is dispalyed in absolute value for better visualization. In all three configurations $\phi_0 = 0.33$, $\phi_r = 0.135$ and $p_c = -0.065$ ($\phi_l = 0.2$).

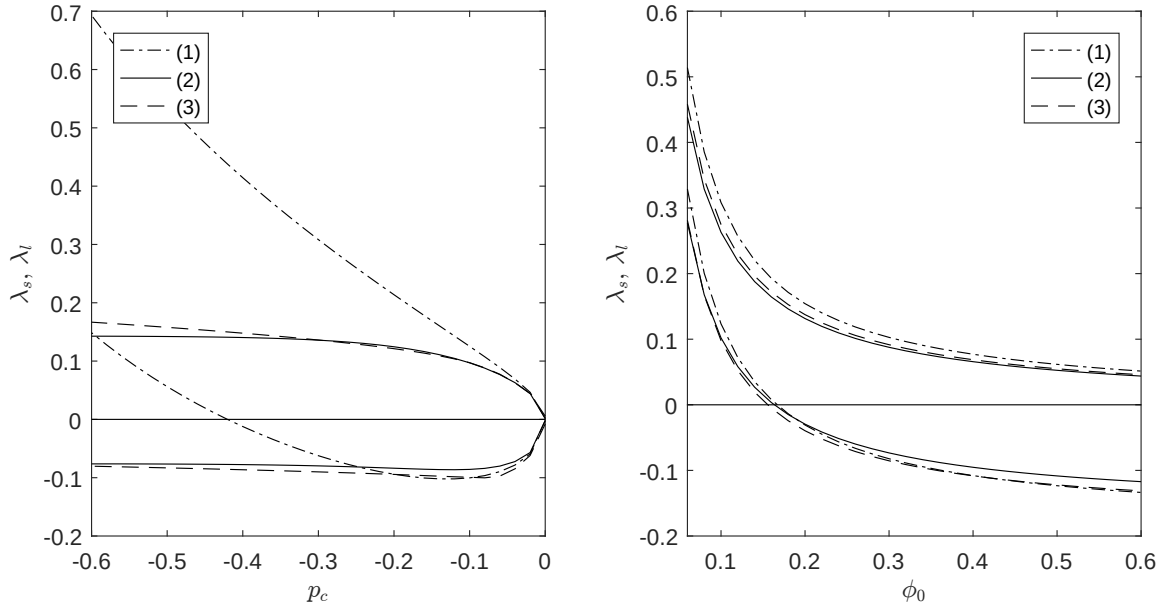

Figure 7: Dependence of the interface positions on p_c (left) and on ϕ_0 (right). The three configurations displayed. $\phi_0 = 0.33$, $\phi_r = 0.135$ and $p_c = -0.065$ - if not varying in the plot.

relative density ρ. In this section, we analyze their effect using the configuration (2), which we pay the strongest attention to.

First (figure 7, left), we took a closer look at the dependence of λ_s, λ_l on the dimensionless capillary pressure p_c. For zero capillary pressure, no imbibition takes place. Increasing the capillary pressure results initially in faster separation of the interfaces. For high capillary pressures however, the effect of the permeability function is significant, resulting in qualitatively different behavior. We would like to note, that the solid volume fraction of the unsaturated porous material ϕ_0 was held constant. For high capillary pressures, this results in $\phi_0 < \sigma^{-1}(p_c) = \phi_l$, i.e. the saturated porous material at the interface λ_l is more dense than the unsaturated porous material.

Increasing the parameter ϕ_0 (figure 7, right) has almost identical effect in all three configurations. For low values of ϕ_0, propagation of the solid front in the positive z direction is observed in all three cases. This however again corresponds to very low (relatively to ϕ_l) unsaturated porous material densities.

To see the whole picture, we further investigated the whole parameter space of p_c and ϕ_0 and their effect on λ_s. In general, low values of ϕ_0 can result in propagation of the solid front in positive z direction. In other words, materials with high porosity

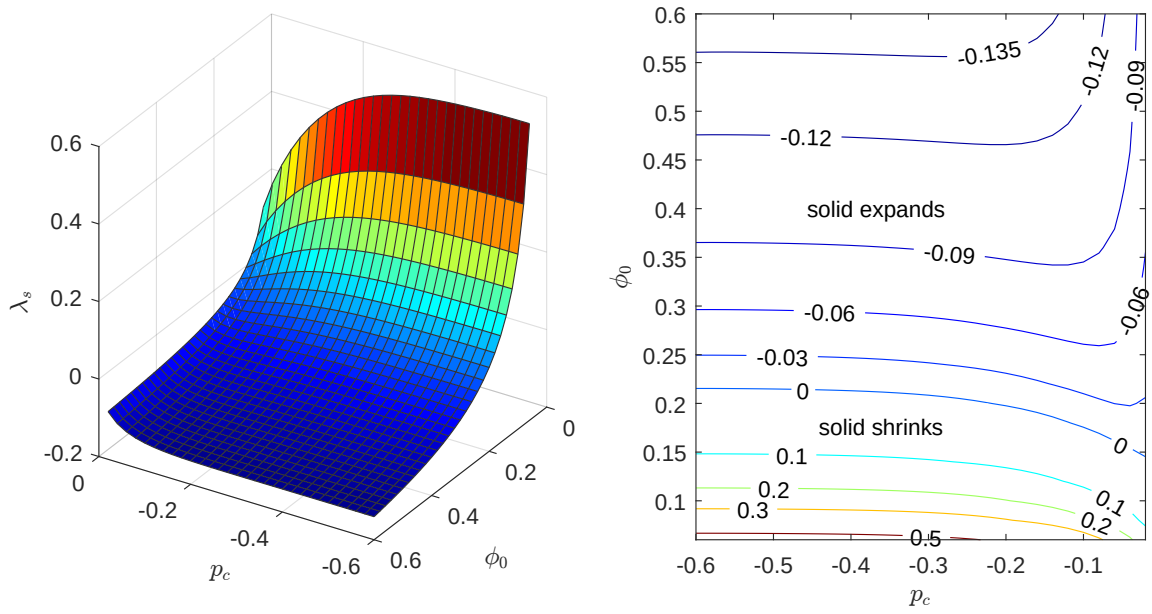

Figure 8: (left) Parametric space of p_c and ϕ_0 and the corresponding values of λ_s. (right) Contour lines of the left plot. $\phi_r = 0.135$.

tend to shrink. To make this physically realistic, we assume that in such cases the liquid stays in contact with the porous material.

3 Steady state

The simplest, yet fundamental case is the steady state. These solutions play an important role in studying the effect of the stress and permeability functions (i.e. the physical properties of the elastic material) on the long-term equilibrium. Furthermore, they provide a useful way of verifying the accuracy and stability of a numerical scheme devised for the nonzero gravity problem.

This whole section will be based on an assumption that a steady state exists. We do not attempt to prove the existence of the steady state to justify this assumption; however, as we shall see in the numerical simulations of the nonzero gravity problem a steady state is always reached and this assumption is reasonable. From a physical viewpoint, it is reasonable to expect that at some point gravity will get into balance with pressure gradient driving the flow.

3.1 Governing equations

Assuming existence of a steady state, we set all terms containing time-derivative to zero, which results in a significant simplification of the governing equations. Equation (1.26) reduces to

$$\frac{\partial p}{\partial z} + 1 = 0, \tag{3.1}$$

which can be in turn used in (1.27) to obtain an ODE for steady-state solid volume fraction

$$\sigma'(\phi)\frac{\mathrm{d}\phi}{\mathrm{d}z} - \rho\phi = 0, \qquad h_s^\infty \leq z \leq h_l^\infty. \tag{3.2}$$

However, we need to determine the interface positions h_s^∞ and h_l^∞ together with some initial or terminal condition. We begin by noting that $\phi(h_s^\infty) = \phi_r$, since this value is constant at all times. By integrating (3.1) and using boundary conditions (1.21), (1.28), we find h_l^∞ at which the pressure gradient is in balance with the nondimensionalized gravity force

$$h_l^\infty = -p_c. \tag{3.3}$$

To determine boundary value $\phi_l^\infty = \phi(h_l^\infty)$, we employ a simple assumption, that the mass of the porous material remains the same throughout the imbibition. At $t = 0$, the mass of the dry porous material that will eventually be wetted through the process

equals $\phi_0 \rho_s^{*T} h_l^\infty$ (ϕ_0 and ρ_s^{*T} are the solid fraction and true densities of the dry porous material respectively). At steady state, this mass is given by the spatial integral of the solid volume fraction $\rho_s^{*T} \int_{h_s^\infty}^{h_l^\infty} \phi(z) \mathrm{d}z$. In other words

$$h_l^\infty \phi_0 = \int_{h_s^\infty}^{h_l^\infty} \phi(z) \mathrm{d}z. \tag{3.4}$$

Integrating (3.2) and comparing with (3.4) gives an implicit equation for ϕ_l^∞

$$h_l^\infty \phi_0 = \int_{h_s^\infty}^{h_l^\infty} \phi(z) \mathrm{d}z = \frac{1}{\rho} \int_{\phi_r}^{\phi_l^\infty} \sigma'(\phi) \mathrm{d}\phi = \frac{\sigma(\phi_l^\infty)}{\rho}. \tag{3.5}$$

Having obtained the position of h_l^∞ and the function value at this point ϕ_l^∞, we can numerically integrate the ordinary differential equation (3.2) to determine the steady-state profile $\phi(z)$ as well as the (not yet determined) solid interface position h_s^∞

$$\rho(h_l^\infty - h_s^\infty) = \int_{h_s^\infty}^{h_l^\infty} \frac{\sigma'(\phi)}{\phi} \frac{\mathrm{d}\phi}{\mathrm{d}z} \mathrm{d}z = \int_{\phi_r}^{\phi_l^\infty} \frac{\sigma'(\phi)}{\phi} \mathrm{d}\phi. \tag{3.6}$$

Note that the steady-state solution is independent of the choice of the permeability function $k(\phi)$. This means that the permeability function has an effect only on the temporal distribution of the solid and liquid phases by governing the speed of imbibition at various solid volume fractions. In the long run however, the equilibrium is reached by balancing the pressure, stress and gravity.

Another qualitative conclusion about the steady-state solid–liquid distribution can be drawn from equation (3.2)

$$\frac{\mathrm{d}\phi}{\mathrm{d}z} = \rho \frac{\phi}{\sigma'(\phi)}. \tag{3.7}$$

Since $\phi > 0$ and σ' is assumed to be negative throughout the wetted region, the increasing/decreasing character of ϕ depends entirely on ρ. Recall, that $\rho = \left(\rho_s^{*T}/\rho_l^{*T} - 1\right)$, implying that $\rho > 0$ for $\rho_s^{*T} > \rho_l^{*T}$ and $\rho < 0$ for $\rho_s^{*T} < \rho_l^{*T}$. For $\rho_s^{*T} > \rho_l^{*T}$, $\frac{\mathrm{d}\phi}{\mathrm{d}z} < 0$, meaning that at steady state, the more dense solid phase tends to accumulate at the bottom. The converse holds for $\rho_s^{*T} < \rho_l^{*T}$.

The position of liquid front interface h_l^∞ is linearly dependent on the capillary pressure p_c. The apparent dependence on the representative scale Σ_0 and thus on the stress

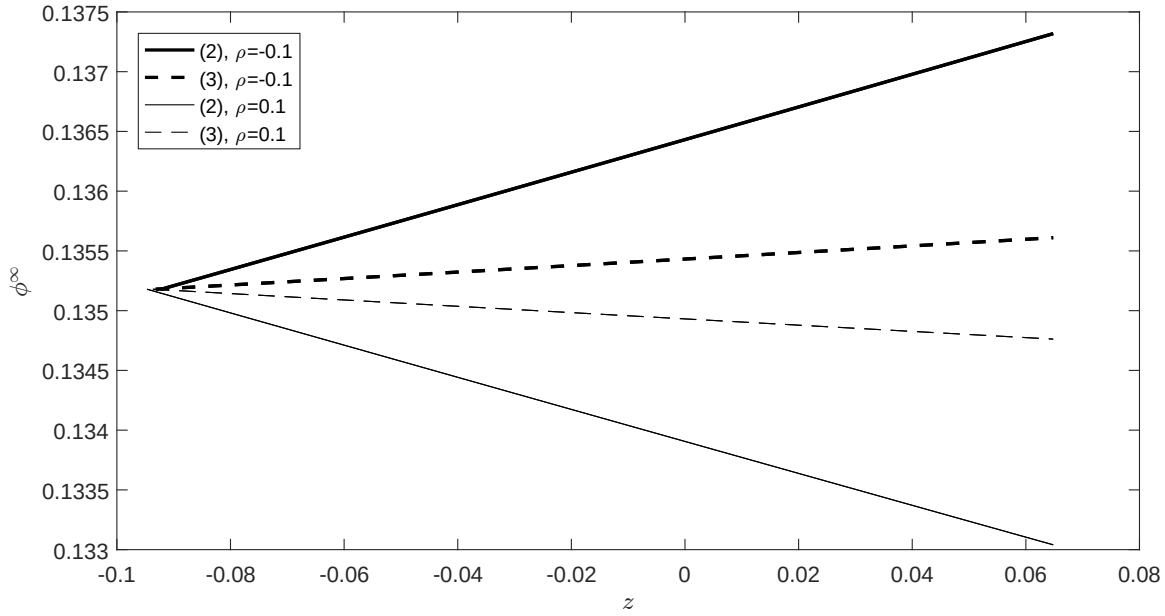

Figure 9: Steady-state profiles $\phi(z)$ for configuration (2) and (3) for denser solid phase (ρ¿0) and denser liquid phase $\rho < 0$.

function is not observed in the dimensional world, since $L^* = \Sigma_0^*/\rho_l^{*T} g^*$, resulting in

$$h_l^{*\infty} = L^* h_l^\infty = -\frac{p_c^*}{\rho_l^{*T} g^*}. \tag{3.8}$$

The dimensional position of the liquid front $h_l^{*\infty}$ therefore depends only on the capillary pressure and density of the liquid. Multiplying both sides by ρ_l^{*T} (and some averaged liquid volume fraction) gives us a simplified interpretation of this equation: the total gravity force exerted on the liquid imbibed is in balance with the capillary pressure acting on the boundary.

3.2 Solutions

Similarly to the previous section, we first show sample plots of the ϕ profile. However, only for two configurations, since the different permeability functions in configurations (1) and (2) do not play a role.

Figure 9 displays the steady-state solutions for the linear stress function (solid line) and 7^{th} degree polynomial stress function (dashed line). In both cases, the steady-state solutions are fairly linear, with $\phi(h_s^\infty) = \phi_r$. The character of the function is mainly influenced by $\phi(h_l^\infty) = \sigma^{-1}(-\rho\phi_0 p_c)$. As expected, in the case of relatively denser solid

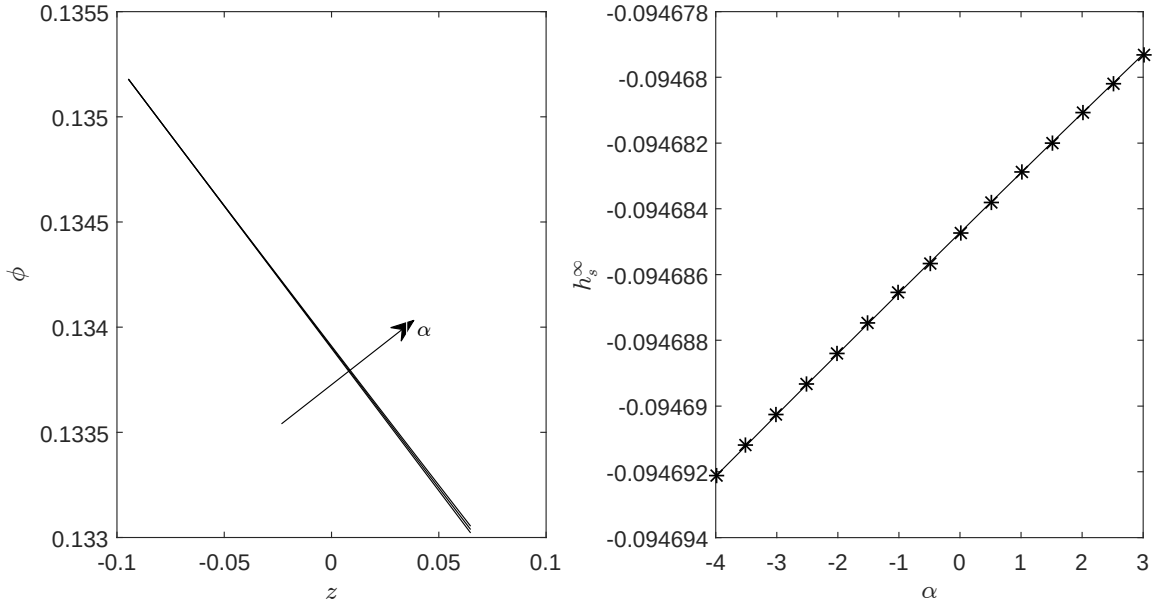

Figure 10: Dependence of the steady-state solid deformation given by h_s^∞ on the parameter α. $\phi_0 = 0.33$, $\phi_r = 0.135$, $p_c = -0.065$ and $\rho = 0.1$.

phase ($\rho > 0$), the solid phase accumulates near the bottom, in the case of relatively denser liquid phase ($\rho < 0$), the solid phase accumulates near the top. The steady-state interface positions are given by the domain of the respective profiles, i.e. little difference between the stress functions is observed.

3.2.1 Parametric class of stress and permeability functions

The permeability function has no effect on the steady state. The effect of the parameter α of the quadratic stress function on the solid front position h_s^∞ can be easily expressed analytically

$$h_s^\infty = -(1 + 2\alpha\phi_r) \ln\left(1 + \frac{1 - \sqrt{1 - 4\alpha\rho\phi_0 p_c}}{2\alpha\phi_r}\right) + 2\alpha\left(\frac{1 - \sqrt{1 - 4\alpha\rho\phi_0 p_c}}{2\alpha\phi_r}\right) \tag{3.9}$$

and is of order 10^{-5}, which is practically unobservable. The reason of such a small dependence can be seen in the equation (3.6), where the upper bound of integration is $\phi_l = \sigma^{-1}(-\rho\phi_0 p_c) \approx \sigma^{-1}(0.002)$, which is a value very close to ϕ_r. In this region, the contribution of the quadratic correction is negligible.

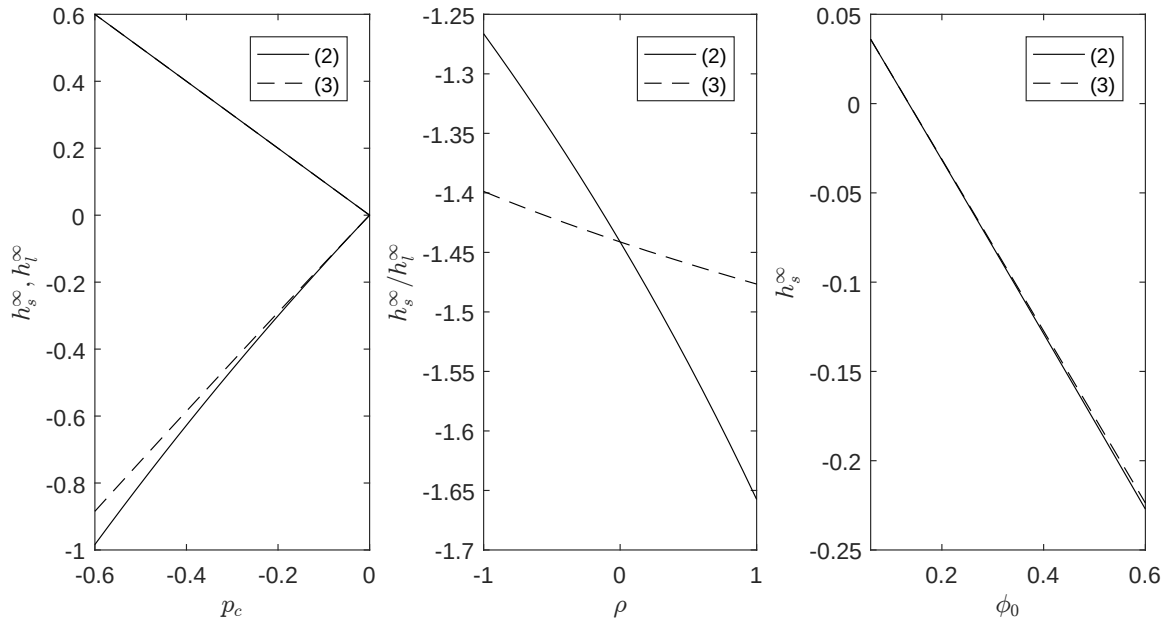

Figure 11: Dependence on the remaining parameters. $\phi_0 = 0.33$, $\phi_r = 0.135$, $p_c = -0.065$ and $\rho = 0.1$ (unless one of the parameters is changing in the plot).

3.2.2 Dependence on parameters ϕ_0, p_c and ρ

Figure 11 (left) shows the dependence of the solid and liquid front positions on the nondimensionalized capillary pressure p_c. For $p_c = 0$, no imbibition or solid deformation takes place. For increasing capillary pressure, both interfaces evolve in a relatively linear way ($h_l^\infty = -p_c$). The middle plot shows the relative deformation as a function of the density parameter ρ. Increasing this parameter, i.e. the relative solid density, results in a higher relative solid deformation. Finally, the solid front interface h_s^∞ also depends on ϕ_0 (right). Again, for low values of ϕ_0, shrinkage of the solid material is observed.

Figure 12 shows the parameter space of p_c and ϕ_0 in a similar way as figure 10.

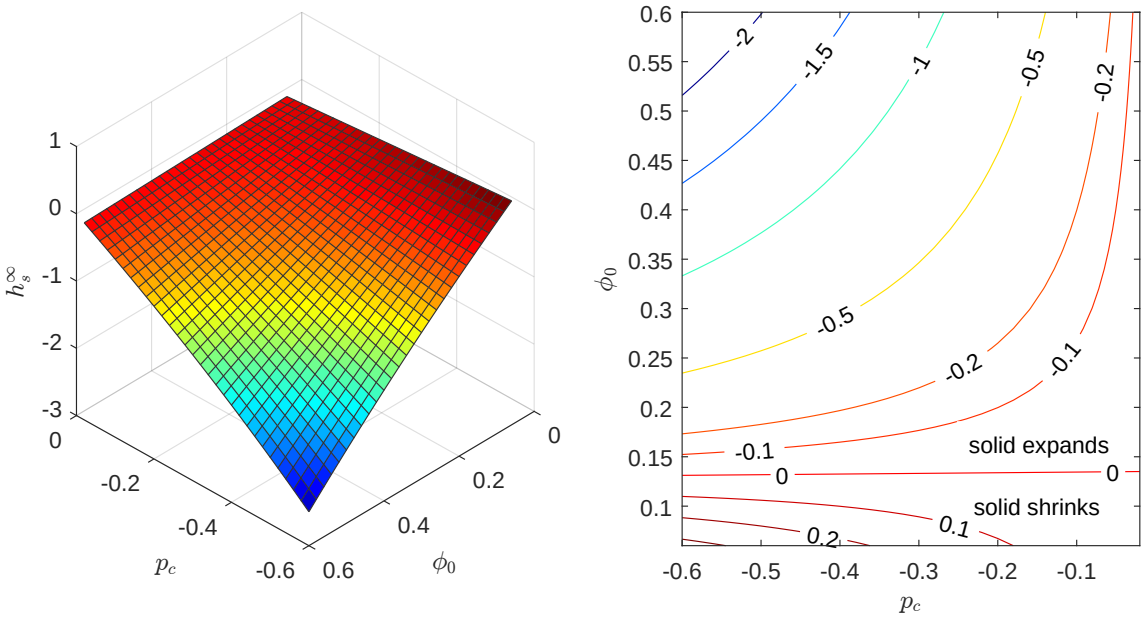

Figure 12: (left) Parametric space of p_c and ϕ_0 and the corresponding values of λ_s. (right) Contour lines of the left plot. $\phi_r = 0.135$ and $\rho = 0.1$.

4 Nonzero gravity

We now turn to the problem of solving the time-dependent problem with gravity field present as described in section 1. The numerical implementation employs the method of lines with pseudospectral and finite difference spatial discretizations. The resulting nonlinear system of initial value problems is solved using the MATLAB built-in solver *ode23s*. For the initial profile $\phi(z, t_0)$ for $t_0 << 1$, we use the correspondingly rescaled self-similar solution described in section 2.

Before we can employ the method of lines; however, we need to formulate the boundary conditions in form of time-dependent ODEs. From the zero-stress condition, $\phi(h_s(t), t) = \phi_r$, i.e. the material at the solid/liquid interface is relaxed at all times. At $h_l(t)$ however, ϕ is not expected to be constant and we denote this quantity $\psi(t) := \phi(h_l(t), t)$. We would like to derive an ODE governing the dynamics of ψ in order to implement it in the method of lines. We restate here the boundary condition (1.49)

$$p_c + h_s(t) = \sigma(h_l(t), t) - \int_{h_s(t)}^{h_l(t)} (\rho\phi + 1)\mathrm{d}z, \tag{4.1}$$

which holds for every $t > 0$. By differentiating this equation with respect to time and noting that $\sigma(h_l(t), t) = \sigma(\psi(t))$ we obtain

$$\dot{h_s}(t) = \sigma'(\psi(t))\dot{\psi}(t) - \frac{\mathrm{d}}{\mathrm{d}t}\int_{h_s(t)}^{h_l(t)} (\rho\phi - 1)\mathrm{d}z. \tag{4.2}$$

We use the following theorem from elementary calculus to differentiate parametric integral with time-dependent bounds

$$\frac{\mathrm{d}}{\mathrm{d}t}\int_{\alpha(t)}^{\beta(t)} f(x,t)\mathrm{d}x = \int_{\alpha(t)}^{\beta(t)} \frac{\partial}{\partial t} f(x,t)\mathrm{d}x + \dot{\alpha}(t)f(\alpha(t),t) - \dot{\beta}(t)f(\beta(t),t). \tag{4.3}$$

Applying this to our equation (4.2) and rearranging gives

$$\sigma'(\psi(t))\dot{\psi}(t) = \rho\int_{h_s(t)}^{h_l(t)} \frac{\partial\phi}{\partial t}\mathrm{d}z + \dot{h_s}(t) + \dot{h_l}(t)(\rho\psi(t) - 1) - \dot{h_s}(t)(\rho\phi_r - 1) \tag{4.4}$$

$\frac{\partial\phi}{\partial t}$ can be substituted from the partial differential equation (1.43) or equivalently from the equation for mass conversation of solid phase (1.24), which requires less equation

manipulation

$$\int_{h_s(t)}^{h_l(t)} \frac{\partial \phi}{\partial t} \mathrm{d}z = \int_{h_s(t)}^{h_l(t)} \frac{\partial}{\partial z}\big(\phi v_s\big)\mathrm{d}z = \big(\phi v_s\big)\big|_{h_s}^{h_l}. \tag{4.5}$$

To evaluate v_s at h_l, we use equation (1.30)

$$v_s = \frac{1}{\phi}\big(c - v_l(1-\phi)\big), \tag{4.6}$$

which results in

$$\int_{h_s(t)}^{h_l(t)} \frac{\partial \phi}{\partial t} \mathrm{d}z = \int_{h_s(t)}^{h_l(t)} \frac{\partial}{\partial z}\big(\phi v_s\big)\mathrm{d}z = \big(c - v_l(1-\phi)\big)\big|_{h_l} - \big(\phi v_s\big)\big|_{h_s} = \phi_r \dot{h_s} - c + \dot{h_l}(1-\psi). \tag{4.7}$$

Putting equations (4.6) and (4.9) together after some manipulation results in a simple equation governing the evolution of the solid volume fraction at boundary h_l

$$\dot{\psi} = \frac{1}{\sigma'(\psi)}\left[\dot{h_l}\big(1+\rho\big) - \rho c\right]. \tag{4.8}$$

The numerical scheme is described in detail in section 5.

For early times when gravity effects are negligible compared to the pressure gradient, we expect the solution to follow the zero-gravity case. For later times; however, the solution should reach the steady state described in section 3. Note that for $\rho > 0$, the initially increasing profile ϕ evolves into slowly decreasing, as shown in the figure 13 for the 7^{th} degree polynomial stress function. The initially highly convex zero-gravity profile also steadies very fast. For $t > 2$, the difference between $\phi(z,t)$ and the steady-state profile was of order 10^{-5}.

4.1 Space of parameters p_c and ϕ_0

In sections 2 and 3, we analyzed the dependence of the solid front position on material parameters p_c and ϕ_0. Putting together this information, three qualitatively different modes of solid front evolution can be expected

1. $h_s(t) < 0$ for $t > 0$,
2. $h_s(t) > 0$ for $t \in (0, t^*)$, $h_s(t) < 0$ for $t \in [t_c, \infty)$ for some $t_c > 0$,
3. $h_s(t) > 0$ for $t > 0$.

Figure 14 shows the space of parameters ϕ_0 and p_c with the three modes and corresponding sample plots of front evolution.

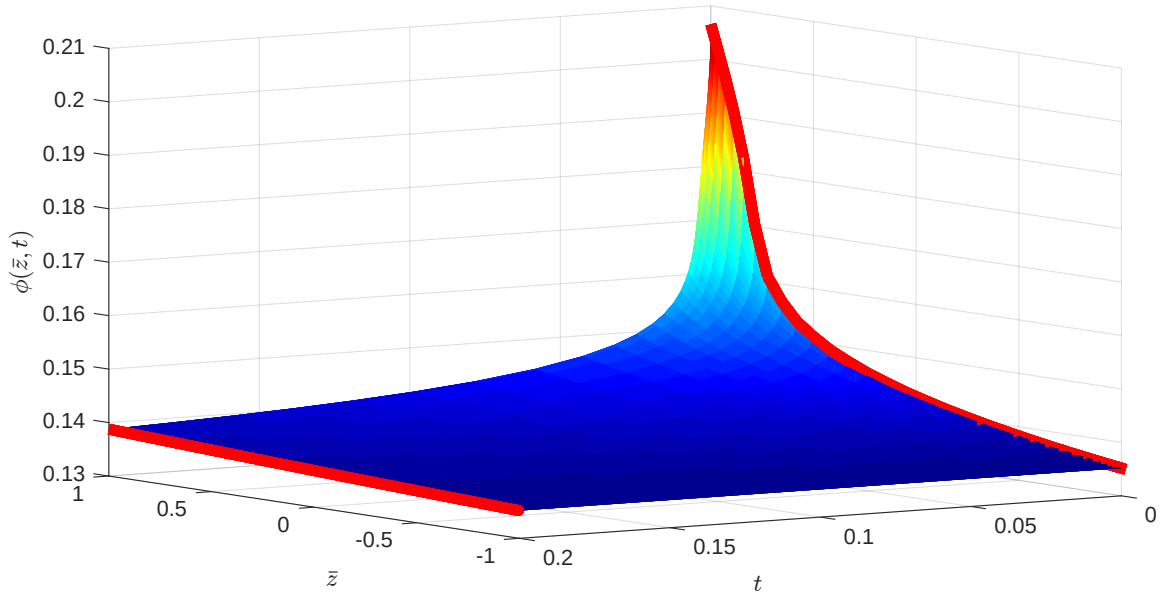

Figure 13: Evolution of the profile $\phi(z,t)$ for the 7^{th} degree polynomial stress function. Initial zero-gravity profile and steady-state profile depicted in red. $\phi_0 = 0.33$, $\phi_r = 0.135$, $p_c = -0.065$ and $\rho = 0.1$.

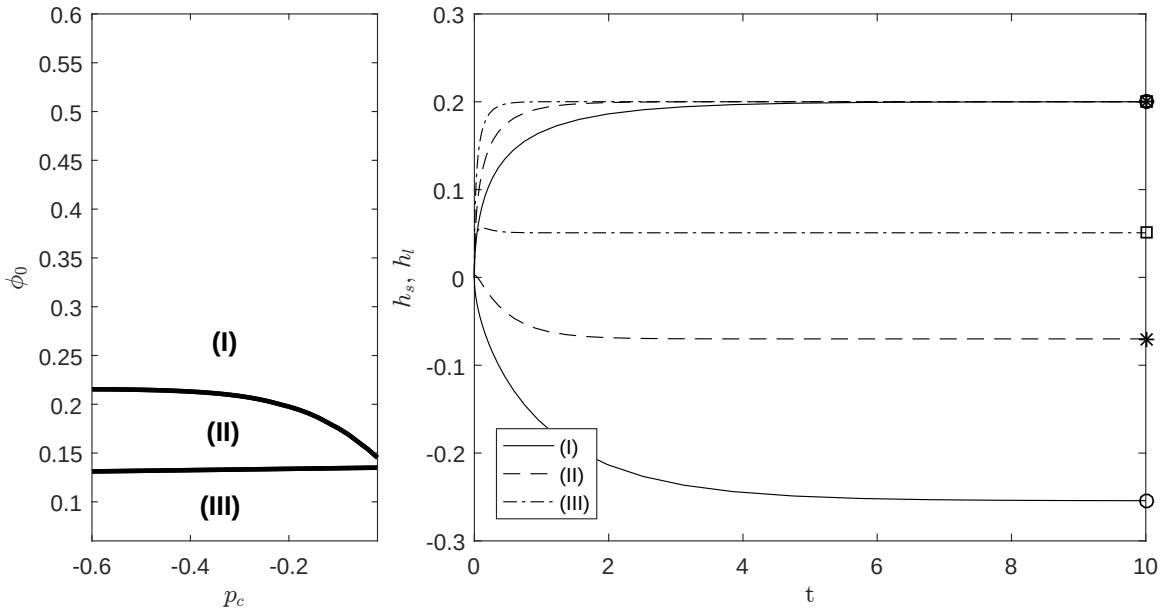

Figure 14: Three modes identified in the space of parameters p_c and ϕ_0 (left) and corresponding time-dependent interface positions together (right) with steady-state positions in the very right. The stress and permeability functions correspond to configuration (2) from subsection 2.2. Mode I: $p_c = -0.2$, $\phi_0 = 0.3$; Mode II: $p_c = -0.2$, $\phi_0 = 0.18$ a Mode III: $p_c = -0.2$, $\phi_0 = 0.1$. $\rho = 0.1$ and $\phi_r = 0.135$ in all modes.

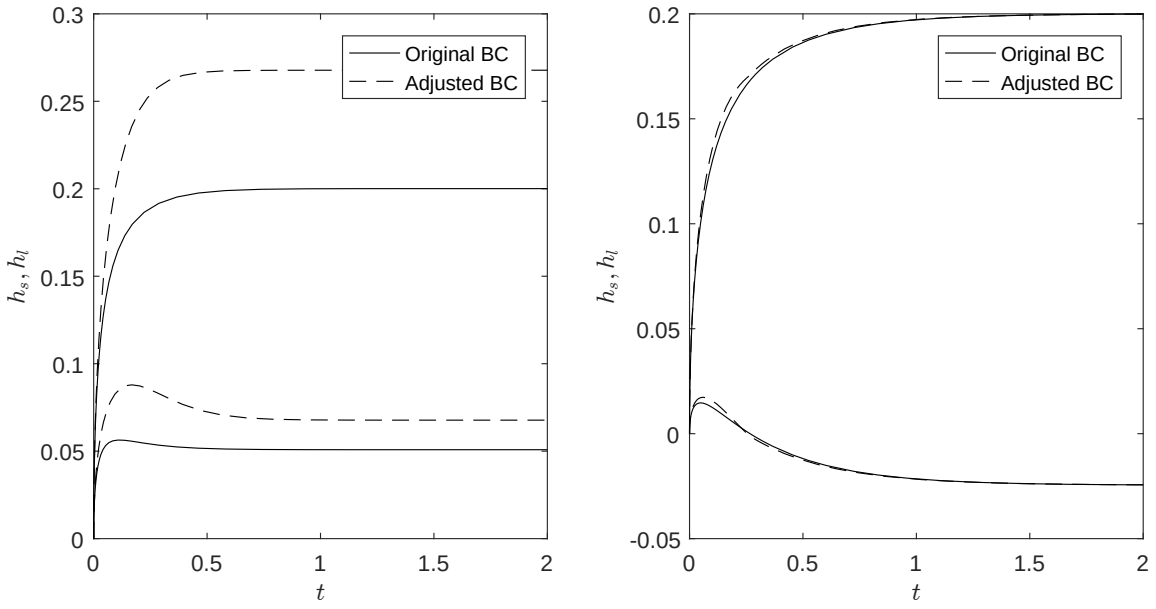

Figure 15: Front positions for the original and adjusted boundary condition. Left: $\phi_0 = 0.1$, resulting in permanently positive h_s and a greater difference. Right: $\phi_0 = 0.18$ resulting in negative final h_s and a smaller difference. $\phi_r = 0.135$, $p_c = -0.2$ and $\rho = 0.1$.

4.2 Adjusted boundary condition

As we already noted, for $h_s > 0$ to be physically realistic, we expect the surface of the liquid bath to remain in contact with the porous material. For such cases; however, the hydrostatic boundary condition in (1.28) is still not very realistic, since it allows for negative hydrostatic pressures. A more realistic boundary condition would be of the form

$$p(h_s^+, t) = p_A - \min(h_s(t), 0). \tag{4.9}$$

Using this in the derivation of the boundary condition for $\psi(t)$ gives

$$\dot{\psi}(t) = \frac{1}{\sigma'(\psi)}\left[\dot{h_l}\big(1+\rho\big) - \rho c - \dot{h_s} + \mathcal{H}(\dot{h_s}, h_s)\right], \tag{4.10}$$

where $\mathcal{H}$ is given by

$$\mathcal{H}(\dot{x}, x) = \begin{cases} 0, & x > 0, \\ \dot{x}, & x \leq 0. \end{cases} \tag{4.11}$$

For $h_s > 0$, this results in slightly higher pressure gradient across the wetted region and thus higher rise of the liquid as displayed in figure 15. The longer the front position h_s is positive, the greater the effect of the adjusted boundary condition.

4.3 Comparison with experimental data

Finally, we compared the theory with the experimental data reported in [9]. As we already mentioned, the authors here investigated a problem with the same setup as described in section 1.2, but used a linear stress function and a linear rational permeability function. They observed an initial dynamics in agreement with the zero-gravity problem, when the fronts follow a $t^{1/2}$ power law. After about 10 s a transition to a power law of about $t^{0.22}$ for the liquid front and $t^{0.20}$ for the solid front was observed. Even afer 10^3 s, no equilibrium was reached.

To transform into dimensional terms, one needs the typical stress and permeability scales Σ_0^* and K_0^*, together with gravity acceleration g^*, liquid density ρ_l^{*T} and fluid viscosity μ^*. The latter parameters g^*, ρ_l^{*T}, μ^* can be easily obtained. To obtain Σ_0^* and K_0^*, one would need to directly measure the stress and permeability functions (as done in [10] for a different setup). The authors in [9] used an inverse approach, which we briefly describe below.

- They experimentally estimated $\phi_0 = 0.1$, $\phi_r = 0.073$ and assumed that there is no jump in the solid volume fraction at the saturated/unsaturated solid interface for the zero-gravity case. In other words $\phi_l = \sigma^{-1}(p_c) = 0.1$. As a corollary, the dimensionless capillary pressure is $p_c = -0.027$.

- Using these values, the zero-gravity solution was computed, resulting in $\lambda_l = 0.3675$ and $\lambda_s = -0.0590$. The dimensional zero-gravity liquid front position is then given by $h_l^*(t^*) = 2\lambda_l\sqrt{\frac{L^{*2}}{T^*}t^*}$.

- The early-time dynamics from experiments was then fitted by $h^*(t^*) = 0.0063\sqrt{t^*}$ [1]. For this to be in agreement with the theoretical prediction from the previous point, the scale ratio L^{*2}/T^{*2} needs to equal $L^{*2}/T^* = 0.0063^2/4\lambda_l^2$.

- The length scale $L^* = 0.7$ m was selected so that the theoretically predicted equilibrium occurs at approximately the time of transition between the power laws.

[1] From several measurements we chose sponge 3 and measurement (7-17), since this measurement was the easiest to resolve from the figures.

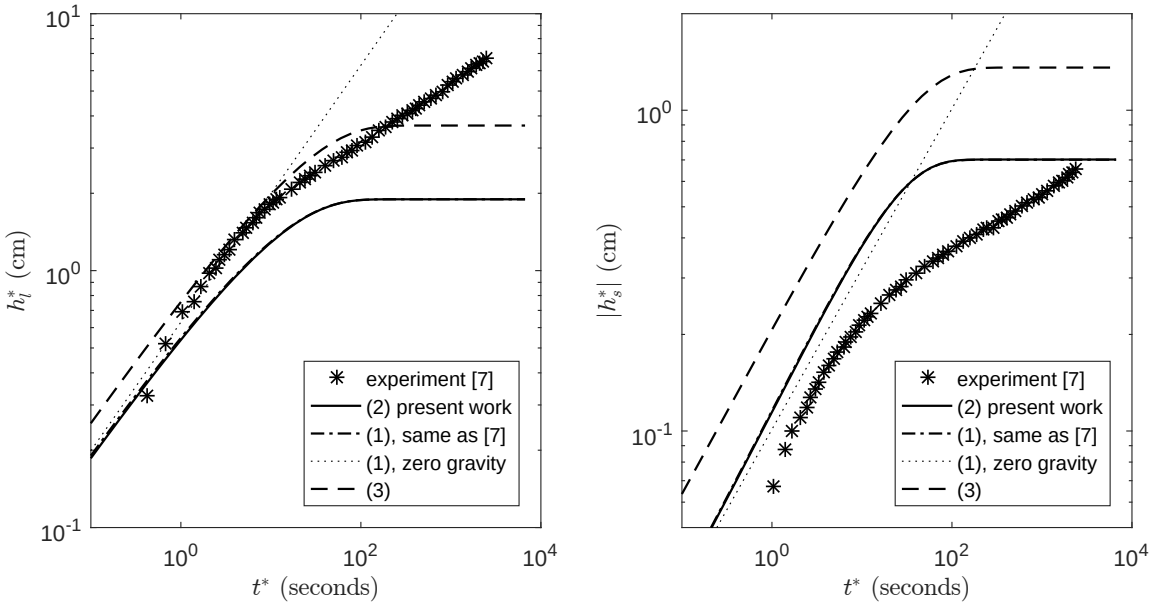

Figure 16: Configurations (1), (2) and (3), experimental measurements from [9] and zero gravity solution for configuration (2).

- As a corollary[2], $T^* = 6.67 \times 10^3$ s, $\Sigma_0^* = 6.87 \times 10^3$ Pa and $K_0^* = 1.07 \times 10^{-11}$ m^2.

Figure 16 displays front positions for the three configurations from the subsection 2.2 against the measurements in [9]. The configuration (1) is the configuration used in [9]. The zero gravity position of h_l^* was used to fit the scale ratio L^{*2}/T^*. The length scale L^* was chosen so that the time of transition between the power laws in the measurements approximately corresponds to the time of transition to the steady state in our model.

Since the stress and permeability scales were not measured directly but fitted to best represent the measurements, it is questionable how to compare the three configurations. We could follow the whole procedure described above and fit the scales for each configuration separately. However, we only assumed that there is no jump in the solid volume fraction at the saturated/unsaturated solid interface as in the first point of the above described procedure. Therefore, L^*, T^* were the same in all configurations.

Furthermore, we would like to note that the results are very sensitive to the parameters considered (figure 17). For instance, a pressure scale $\Sigma_0^* = 2.32 \times 10^3$ Pa (or

[2]Other constants used: $g^* = 9.81$ ms^{-1}, ${\rho_l^*}^T = 10^3$ kgm^{-1}, $\mu^* = 10^{-3}$ kgs^{-1}m^{-1}.

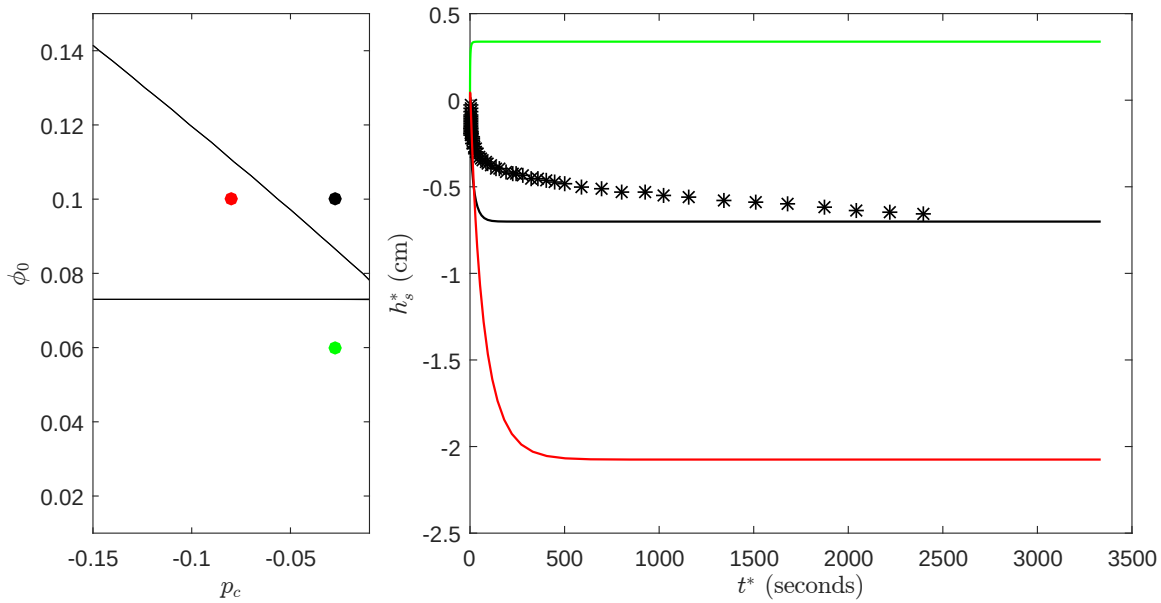

Figure 17: Slight variations of the parameters resulting in qualitatively different bahaviours.

equivalently $\phi_l = 0.18$) could lead to an initial compression of the porous material. Alternatively, a slightly more porous material with $\phi_0 = 0.06$ would lead to permanent compression of the porous material. Thus, such predictions have to be taken conservatively, especially since no direct measurements of stress and permeability were performed.

5 Numerical schemes

In this section, we describe in detail the numerical schemes used to solve the equations in sections 1 through 4.

The equations regarding the steady state in section 3 involve simple, first-order ordinary differential equations and definite integral evaluation. Thus, no special numerical scheme needed to be employed and MATLAB solvers *ode45* and *integral* were used.

In the remaining parts, Chebyshev pseudospectral method was mainly used to numerically approximate the differential operators. This method is known for exponential convergence for smooth functions [12]. The downside is that it involves full differentiation matrices that require longer computation times. Moreover, we encountered that for highly nonlinear stress functions (considered in [10]) and high capillary pressures, the Chebyshev grid (clustered at the endpoints of the domain) seemed to be too coarse in the middle of the domain and high spectral resolutions were required to capture the solution. In such situations, a simpler second-order finite difference scheme worked comparably well.

The Chebyshev pseudospectral approach is most commonly defined on interval $[-1, 1]$, thus the differential equations need to be rescaled to this interval by linear transformation. The solution is a polynomial of $N+1^{st}$ degree represented by a vector of function values $\phi^{CH} = (\phi_0^{CH}, \phi_1^{CH}, \ldots, \phi_{N+1}^{CH})$ corresponding to the function values in so-called Chebyshev nodes $z_j = \cos(\pi j/(N+1))$, $j = 0, \ldots, N+1$. These nodes are quadratically clustered towards the ends of the interval $[-1, 1]$ to avoid effects like the Runge's phenomenon [3]. The solution could be equivalently represented by the coefficients of the polynomial (which would make it a spectral method); however, this approach is more straightforward to implement and is more similar to other gridpoint methods.

Having the function values $\phi^{CH} = (\phi_0^{CH}, \phi_1^{CH}, \ldots, \phi_{N+1}^{CH})$, the polynomial interpolant is of the form

$$\phi(z) = \sum_{i=0}^{N+1} \phi_i^{CH} \ell_i(z), \tag{5.1}$$

where ℓ_i is the Lagrange basis polynomial satisfying $\ell_i(z_j) = \delta_{ij}$. Differentiating such an interpolant can be represented by multiplication of the vector of function values

ϕ^{CH} by so-called differentiation matrix D, whose elements are given by

$$D_i^j = \ell_j'(z_i). \tag{5.2}$$

This is in fact a $(N+2) \times (N+2)$ matrix, where the first row and the first column have index 0.

This is similar to the finite difference method, where differentiation is also represented by multiplication by a sparse matrix with only a few (depending on the order of the method) nonzero diagonals. For the finite difference method of 2^{nd} order, this matrix is given by

$$\begin{cases} D_i^{i-1} = -1/(2h) & i = 1, \ldots, N \\ D_i^{i+1} = 1/(2h) & i = 1, \ldots, N \\ D_i^j = 0 & \text{otherwise,} \end{cases} \tag{5.3}$$

where $h = z_{i+1} - z_i = \text{const.}$ is the grid spacing. In the 0^{th} and $N+1^{st}$ row, we use one-sided second-order derivative approximation. Similarly to the pseudospectral method, we denote the vector of function values $\phi^{FD} = (\phi_0^{FD}, \phi_1^{FD}, \ldots, \phi_{N+1}^{FD})$.

5.1 Zero-gravity case

To solve the equations (2.8)-(2.12) using Chebyshev pseudospectral approach, we first rearrange the equations to a clearer form involving conditions for derivatives on the boundaries and obtain

$$2\eta \frac{\mathrm{d}\phi}{\mathrm{d}\eta} - 2(1-\phi_0)\frac{\mathrm{d}\phi}{\mathrm{d}\eta} = \frac{\mathrm{d}}{\mathrm{d}\eta}\left[\phi k(\phi)\sigma'(\phi)\frac{\mathrm{d}\phi}{\mathrm{d}\eta}\right]. \tag{5.4}$$

$$\left.\frac{\mathrm{d}\phi}{\mathrm{d}\eta}\right|_{\lambda_s} = 2\frac{\phi_0\lambda_l - (\lambda_l - \lambda_s)}{k(\phi_r)\sigma'(\phi_r)} \tag{5.5}$$

$$\left.\frac{\mathrm{d}\phi}{\mathrm{d}\eta}\right|_{\lambda_l} = -\frac{\lambda_l\phi_0(1-\phi_l)}{\phi_l k(\phi_l)\sigma'(\phi_l)}, \tag{5.6}$$

together with boundary conditions $\phi(\lambda_s) = \phi_r$ and $\phi(\lambda_l) = \phi_l$.

Next, we rescale the independent variable $\eta \in [\lambda_s, \lambda_l]$ to a fixed interval $[-1, 1]$ by linear transformation $\bar{\eta} = (2\eta - \lambda_l - \lambda_s)/(\lambda_l - \lambda_s)$. The set of nonlinear equations

corresponding to a rescaled version of (5.4) has the form

$$\left(\frac{(\lambda_l-\lambda_s)(\bar{\eta}_i-1)}{2}+\phi_0\lambda_l\right)\sum_{j=0}^{N+1}D_i^j\phi_j^{CH}$$
$$=\frac{1}{\lambda_l-\lambda_s}\sum_{j=0}^{N+1}D_i^j\left(\phi_j^{CH}k(\phi_j^{CH})\sigma'(\phi_j^{CH})\sum_{k=0}^{N+1}D_j^k\phi_k^{CH}\right), \tag{5.7}$$

for $i=1,\ldots,N$, together with boundary conditions $\phi_{N+1}^{CH}=\phi_r$ and $\phi_0^{CH}=\phi_l$ (the $N+1^{st}$ node corresponds to $\bar{\eta}=-1$ and vice versa).

We first solve the system of nonlinear equations (5.7) using MATLAB built-in solver *fsolve* for an initial guess of parameter values $\lambda_{s_0},\lambda_{l_0}$. Next, we compute the difference of right-hand and left-hands sides of equations (5.5), (5.6), which are after rescaling and numerical approximation of the form

$$\sum_{j=0}^{N+1}D_0^j\phi_j^{CH}+\frac{\lambda_{l_0}\phi_0(\lambda_{l_0}-\lambda_{s_0})(1-\phi_l)}{\phi_l k(\phi_l)\sigma'(\phi_l)}, \tag{5.8}$$

$$\sum_{j=0}^{N+1}D_{N+1}^j\phi_j^{CH}-\frac{(\lambda_{s_0}-\lambda_{l_0}+\phi_0)(\lambda_{l_0}-\lambda_{s_0})}{k(\phi_r)\sigma'(\phi_r)}. \tag{5.9}$$

In an outer *fsolve* routine, we attempt to solve for λ_s^*,λ_l^*, which corresponds to the roots of these equations. This could be in fact simplified into a single system of nonlinear equations (5.7), (5.8) and (5.9). However, as we noted, the former approach using two nested *fsolve* routines turned out to be more stable for nontrivial choices of stress and permeability functions, since it separates two qualitatively different problems. The slight decrease in accuracy or longer computational time of the nested approach does not play an important role here.

Another option is to use MATLAB adaptive solver for boundary value problems *bvp4c* based on finite difference method [8]. This solver can also handle unknown parameters in both the equation as well as boundary conditions. However, for nontrivial stress functions and high capillary pressures, the routine did not converge.

5.1.1 Closed-form solution

To analyze the convergence of the proposed pseudospectral approach and compare it to 2^{nd} order finite difference, we took a closer look at the simple stress a and permeability functions studied in [9]. Except for them being the simplest form of these functions

satisfying the basic properties outlined in subsection 1.3, they also allow us to express the solution in closed-form. The reason can be easily seen in the RHS of equation (5.4), where all the nonlinear terms cancel out and leave a simple second derivative of ϕ. After a little effort [1], the solution can be shown to have the following form

$$\phi(\eta) = \frac{\operatorname{erf}(\lambda_s - B) - \operatorname{erf}(\eta - B)}{\operatorname{erf}(\lambda_s - B) - \operatorname{erf}(\lambda_l - B)}(\phi_l - \phi_r) + \phi_r, \tag{5.10}$$

where $B = (1 - \phi_0)\lambda_l$. Equations (5.5), (5.6) can also be simplified and result in a system of two nonlinear equations, that can be solved separately from the differential equation. Thus, the nested *fsolve* approach is not necessary here.

We used this problem with known analytic solution to verify the accuracy of earlier proposed numerical schemes. As we wanted to analyze the accuracy of the pseudospectral method, we first obtained (numerically) exact values λ_s, λ_l and solved only the equation (5.7) for increasing number of grid points. In these grid points, we then computed the maximum absolute error as shown in figure 18 (left). As expected, the pseudospectral method exhibits exponential convergence while the finite difference method only polynomial.

In figure 19 we took a closer look at the two-dimensional parameter space of parameters $(\lambda_s, \lambda_l) \in [-1, 0] \times [0, 1]$. For each such pair, we solved the equation 5.7 and then computed the corresponding form of (5.8), (5.9) to obtain two surfaces. These two surfaces are the functions we wish to find the root of in the outer *fsolve* routine. Their intersection forms a one-dimensional manifold, where the residuals are equal (to the corresponding vertical-axis value). At the marked blue point, both residuals are zero, meaning we found the right values λ_s^*, λ_l^*. The purpose of this plot is to show that the differences of RHS and LHS in the equations (5.5), (5.6), numerically approximated by (5.8), (5.9), as functions of parameters λ_s, λ_l form a smooth intersecting surfaces. It is therefore reasonable to expect exactly one solution in terms of λ_l, λ_s from an appropriate parameter space.

We would also like to note that for a different choice of stress and permeability functions, a closed-form solution is hard to be expected. If the RHS of eqation (5.4) is nontrivial, it will contain nonlinear functions of ϕ as well as $(\mathrm{d}\phi/\mathrm{d}\eta)^2$ which is a form not often studied in the theory of ordinary differential equations.

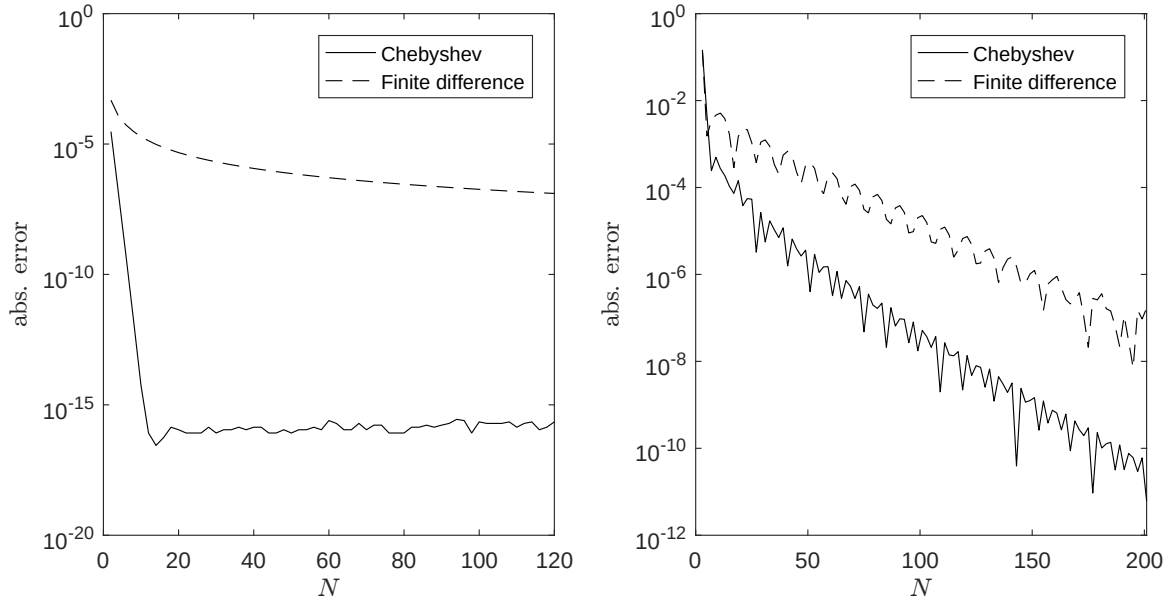

Figure 18: Left: Maximal absolute difference between the analytic solution and solution obtained with N gridpoints for the Chebyshev and finite-difference approach, configuration (1). Right: Absolute difference in the midpoint for two successive resolutions, configuration (3).

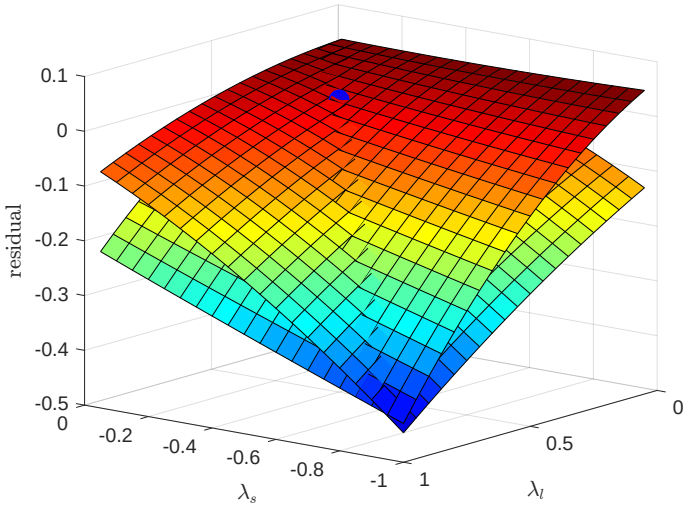

Figure 19: Parameter space (λ_s, λ_l) and the corresponding difference of right-hand and left-hand sides in equations 3.7, 3.8

5.1.2 7th degree polynomial stress function

The case of stress and permeability functions found in [10] results in highly nolinear profiles of $\phi(\eta)$ for high capillary pressures. Here, the Chebyshev grid seemed to be too coarse at the midsection of the interval $[-1, 1]$ for low spectral resolutions.

Figure 18 (right) compares the pseudospectral to the finite difference method. Since an explicit solution to this problem is not known, we had to analyze the relative convergence of the solutions for two successive resolutions N. Another problem we were facing was, that for different resolutions N, the corresponding grids are different and the solutions cannot be directly compared. We tried to interpolate each solution by a cubic spline and compare them on a unified set of points. However, the error of the spline interpolation was of the order comparable to the actual error of the solutions and biased the results. Thus, we used only odd resolutions $N = 2k + 1$ so that the grid (both Chebyshev and finite difference) always includes the point $\bar{\eta}_{(N+3)/2} = 0$ and the absolute difference of function values at this point for two successive values of k was computed. Even though the pseudospectral method converges faster, a qualitative difference, such as in figure 18 (left) is not observed. However, the exponential and polynomial rate of convergence might be present, discernible only at at even higher resolutions.

5.2 Nonzero gravity

To solve the time-dependent problem with gravity field present, we employed the method of lines. In this approach, the partial differential equation (1.43) was transformed into a system of initial value problems. The spatial differential opperator were again discretized using Chebyshev pseudospectral method.

First, the spatial variable z needs to be rescaled to a fixed domain $[-1, 1]$ using linear transformation $\bar{z} = (2z - h_l(t) - h_s(t))/(h_l(t) - h_s(t))$. Note that this transformation is time-dependent, which nontrivially transforms the time derivative to

$$\frac{\partial \phi}{\partial t} = \frac{\partial \bar{\phi}}{\partial t} + \left[\frac{\bar{z} - 1}{h_l - h_s} \frac{\mathrm{d}h_s}{\mathrm{d}t} - \frac{\bar{z} + 1}{h_l - h_s} \frac{\mathrm{d}h_l}{\mathrm{d}t} \right] \frac{\partial \bar{\phi}}{\partial \bar{z}}. \tag{5.11}$$

In the next step, we discretize the spatial variable to discrete Chebyshev nodes $\bar{z}_j = \cos(\pi j/(N + 1))$, $j = 0, \ldots, N + 1$ and introduce new functions dependent solely

on time

$$\varphi_i(t) := \phi(\bar{z}_i, t), \quad i = 0, \dots, N+1. \tag{5.12}$$

The derivative with respect to $\bar{z}$ is now approximated using the differentiation matrix D as

$$\left.\frac{\mathrm{d}\phi}{\mathrm{d}\bar{z}}\right|_{\bar{z}_i} = \sum_{j=0}^{N+1} D_i^j \varphi_j. \tag{5.13}$$

Thus, the rescaled and discretized system of equations (1.43)-(1.46) ammounts to a system of ordinary differential equations

$$\dot{\varphi_i}(t) = -\frac{1}{h_l - h_s}\Big((\bar{z}_i - 1)\dot{h_s} + (\bar{z}_i + 1)\dot{h_l} + 2c\Big)\sum_{j=0}^{N+1} D_i^j \varphi_j \tag{5.14}$$

$$- \frac{2}{h_l - h_s}\sum_{j=0}^{N+1} D_i^j \Big[\varphi_j k(\varphi_j)\frac{2\sigma'(\varphi_j)}{h_l - h_s}\Big(- \rho\varphi_j + \sum_{k=0}^{N+1} D_j^k \varphi_k\Big)\Big], \tag{5.15}$$

$i = 1, \dots, N$ where

$$c(t) = -\frac{1-\phi_0}{\phi_0}\left[\frac{\varphi_0 k(\varphi_0)}{1-\varphi_0}\left(\frac{2\sigma'(\varphi_0)}{h_l - h_s}\Big(- \rho\varphi_0 + \sum_{j=0}^{N+1} D_0^j \varphi_j\Big)\right)\right]. \tag{5.16}$$

Boundary values are given by equations

$$\dot{\varphi}_{N+1}(t) = 0, \tag{5.17}$$

$$\dot{\varphi}_0(t) = \frac{1}{\sigma'(\varphi_0)}\big[\dot{h}_l(1+\rho) - \rho c\big]. \tag{5.18}$$

Finally, the interface position are governed by

$$\dot{h}_s(t) = c + k(\varphi_{N+1})\left[\frac{2\sigma'(\varphi_{N+1})}{h_l - h_s}\Big(- \rho\varphi_{N+1} + \sum_{j=0}^{N+1} D_{N+1}^j \varphi_j\Big)\right], \tag{5.19}$$

$$\dot{h}_l(t) = c - \frac{\varphi_0 k(\varphi_0)}{1-\varphi_0}\left[\frac{2\sigma'(\varphi_0)}{h_l - h_s}\Big(- \rho\varphi_0 + \sum_{j=0}^{N+1} D_0^j \varphi_j\Big)\right]. \tag{5.20}$$

For initial condition, we use the self-similar profile obtained in the zero-gravity case

$$\varphi_i(t_0) = \phi_i^{CH}, \quad i = 0, 1, \dots, N+1, \tag{5.21}$$

where $t_0 << 1$, together with the initial interface positions

$$h_s(t_0) = 2\lambda_s\sqrt{t_0}, \quad h_l(t_0) = 2\lambda_l\sqrt{t_0}. \tag{5.22}$$

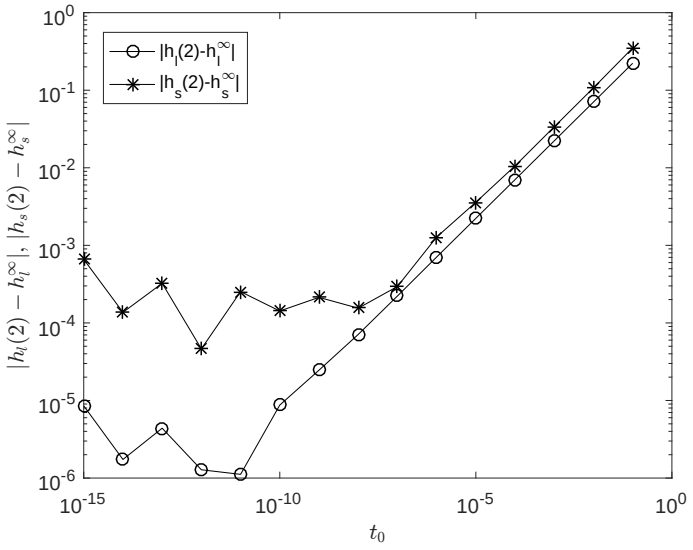

Figure 20: Convergence of $h_s(2)$ and $h_l(2)$ (effective steady states) to the real steady-state values h_s^∞ and h_l^∞ for decreasing initial time t_0. The apparently worse convergence of h_s rests in numerically computed value h_s^∞, whereas $h_l^\infty = -p_c$.

To solve this nonlinear system of initial value problems, we employed the built-in MATLAB solver *ode23s*.

For well resolved self-similar profile $\phi(\eta)$, acting as an initial profile for the method of lines, the convergence to the steady state is largely dependent on the initial time t_0 (the method still converges even for different initial times t_0, but to a different solution). The following figure 20 displays this dependence for the simple stress and permeability functions. Following this result, in most of the plots regarding the nonzero gravity problem in this thesis, we used $t_0 = 10^{-8}$.

Conclusion

In our thesis we have studied a model for imbibition of a liquid into deformable porous material. We have used mixture theory approach described in [5]. Previous existing studies of this problem considered a linear stress function governing deformation of the porous material and a linear rational permeability function dictating the dynamics of imbibition [9]. Experimental work of Sommer and Mortensen [10] indicates a more complex dependence of these quantities on the solid volume fraction of the porous material. Using the experimentally motivated constitutive relations for solid stress and permeability functions, we have investigated a parametric class of exponentially decreasing permeability functions and linear stress functions with a quadratic correction.

In the first section, we have derived a mathematical model using mixture theory and mass and momentum balances following [5]. After reducing to one spatial dimension, we have introduced physically realistic class of stress and permeability functions directly depending on the solid volume fraction ϕ.

In the second section, we have taken a closer look at a further reduction, namely the case with absent gravity field. For the resulting boundary value problem with unknown parameters determining the boundaries, we have developed a numerical scheme based on Chebyshev pseudospectral as well as finite difference discretizations. The resulting nonlinear system of equations was solved using the nested *fsolve* routines. We have investigated the effect of the parameters of stress and permeability functions on the solutions. In addition, we have investigated the effects of other parameters such as the dimensionless capillary pressure p_c and solid volume fraction of the dry porous material ϕ_0. We have found that for certain combination of these parameters, shrinkage, instead of expansion of the porous material occurs.

The third section was devoted to the study of the steady state. Again, we have studied the effect of the parameter of the stress function, which was negligible. The permeability function was found to have no effect on the steady state, since it dictates only temporal speed of liquid infiltration. In the space of material parameters p_c and ϕ_0, again both shrinkage as well as expansion are possible.

In the fourth section, we have studied the general time-dependent problem with gravity present. It connects the early-time dynamics, which is asymptotically equiv-

alent to the zero-gravity case, with the steady-state solution. Based on this, we have identified three qualitatively different modes of the solid phase behavior: initial shrinkage and final expansion of the porous material, permanent shrinkage of the porous material and permanent expansion of the porous material. To make the case when the porous material shrinks more realistic, we have made a slight adjustment to the condition of hydrostatic pressure at one boundary. This adjustment has led to both greater shrinkage and higher liquid rise. Numerically, this problem was implemented using the method of lines with the Chebyshev pseudospectral as well as finite difference spatial discretizations.

In [9], experimental measurements of imbibition of a liquid into a sponge were reported. The main shortcoming of the current model is that even after thousands of seconds, no steady state predicted by the model is observed. Wider and more physically realistic class of stress and permeability functions did not eliminate this problem. One of the main reasons of the discrepancy between the experimental data and the theory might rest in not considering a gas phase in the model. The current model considers the liquid volume to be a full complement to the solid volume in the saturated region. According to [9], the actual liquid volume in the saturated region is considerably smaller than the void pore space, i.e. air and liquid vapor are present. Including a gas phase in the model might be an interesting direction of future research.

References

[1] D. M. Anderson, *Imbibition of a liquid droplet on a deformable porous substrate*, Physics of Fluids, 17 (2005).

[2] S. I. Barry and G. K. Aldis, *Radial flow through deformable porous shells*, Journal of the Australian Mathematical Society, 34 (1993), pp. 333–354.

[3] B. Fornberg, *A Practical Guide to Pseudospectral Methods*, Cambridge University Press, Cambridge, 1996.

[4] P. Guba and D. M. Anderson, *Diffusive and phase change instabilities in a ternary mushy layer*, J. Fluid Mech., 760 (2014), pp. 634–669.

[5] R. Masoodi and K. M. Pillai, *Wicking in Porous Materials: Traditional and Modern Modeling Approaches*, CRC Press, Boca Raton, 2012.

[6] D. A. Nield and A. Bejan, *Convection in porous media*, Springer, Cambridge, 1992.

[7] L. Preziosi, D. D. Joseph, and G. S. Beavers, *Infiltration of initially dry, deformable porous medial*, International Journal of Multiphase Flow, 22 (1996), pp. 1205–1222.

[8] L. F. Shampine, J. Kierzenka, and M. W. Reichelt, *Solving boundary value problems for ordinary differential equations in matlab with bvp4c*, (2000).

[9] J. I. Siddique, D. M. Anderson, and A. Bondarev, *Capillary rise of a liquid into a deformable porous material*, Physics of Fluids, 21 (2009).

[10] J. L. Sommer and A. Mortensen, *Forced unidirectional infiltration of deformable porous media*, Journal of Fluid Mechanics, 331 (1996), pp. 193–217.

[11] S.Whitaker, *Flow in porous media I: A Theoretical Derivation of Darcy's Law*, Transport in porous media, 1 (1986), pp. 3–25.

[12] L. N. Trefethen, *Spectral Methods in MATLAB*, Cambridge University Press, Cambridge, 1996.

Appendix A Code listing

In this appendix, we list the MATLAB codes used to solve the zero-gravity, steady-state and nonzero-gravity problems. To construct the Chebyshev differentiation matrix, we have used a very terse function *cheb* introduced [12]. The functions `SelfSimilar` and `TimeDependent` can optionally accept input arguments for initial guess of parameters λ_s, λ_l and initial profile ϕ. If no optional input arguments are passed, initial guess for parameters is $\lambda_s = -0.5, \lambda_l = 0.5$ and the initial profile is linear satisfying boundary conditions.

Listing 1: MATLAB source code for the zero-gravity problem

```
%%%%%%%%%%%%%%%%%%%%%%%%%%%%%%%%%%%%%%%%%%%%%%%%%%%%%%%%%%%%%%%%%%%%%%%%%%%%%%%
function sol = SelfSimilar(s, N, approach, lambda_init, phi_init)
% solves eqns (2.7)-(2.10) using nested fsolve routines
% s...structure of problem settings (s.phi0, s.phir, s.rho, s.pcs, anonymous functions s.K, s.Sigma, s.Sigmap ...)
% N...number of (inner) grid points
% approach...'cheb' - Chebyshev differentiantion matrix
%          ...'fd' - finite difference differentiation amtrix
% lambda_init...(optional) initial guess for parameters, [0.5,-0.5] if not specified
% phi_init...(optional) anonymous function for initial profile of phi, linear function
%            satisfying the BCs if not specified

% pseudespectral OR finite difference approach, see fcns cheb and fd
global D ksi                    % differentiation matrix, nodes as global
switch approach
    case 'cheb'
        [D,ksi] = cheb(N+1);    % N+2 - length incl. boundary values
        ksi = wrev(ksi);        % revert order of cheb. nodes for clarity
        D = -D;                 % revert diff. matrix for the same reason
    case 'fd'
        [D,ksi] = fd(N+1);
    otherwise
        disp('wrong method chosen')
        return
end

% compute value at boundary ksi=+1 (condition (2.12))
bvplus = @(x) s.pcs - s.Sigma(x);
s.phil = fsolve(bvplus, (s.phir-s.pcs));

% initial guesses for phi and lambda
switch nargin
    case 3
        linear_guess = @(t) (s.phil-s.phir)/2*t + (s.phir+s.phil)/2;
        init_guess = linear_guess(ksi(2:N+1));
        lambda_init = [0.5,-0.5];
    case 4
        linear_guess = @(t) (s.phil-s.phir)/2*t + (s.phir+s.phil)/2;
        init_guess = linear_guess(ksi(2:N+1));
    case 5
        init_guess = phi_init(ksi(2:N+1));
    otherwise
        disp('incorrect number of input arguments to the function SelfSimilar');
```

```
        return
end

% objective function for solving equations (2.9), (2.10)
obj_fun = @(lambda) FixedLambdas(lambda(1), lambda(2), s, N, init_guess);
[lambda] = fsolve(obj_fun, lambda_init);

% construct output structure
l_l = lambda(1);
l_s = lambda(2);
[ders_diff, phi_sol] = FixedLambdas(l_l, l_s, s, N, init_guess);
sol = struct('lambda_s', l_s, 'lambda_l', l_l, 'phi', phi_sol, 'grid', ksi, 'ders_diff', ders_diff);
end

%%%%%%%%%%%%%%%%%%%%%%%%%%%%%%%%%%%%%%%%%%%%%%%%%%%%%%%%%%%%%%%%%%%%%%%%%%%%%%%
function [ders_diff, phi_sol] = FixedLambdas(l_l, l_s, s, N, init_guess)
% solves equation (2.8) given (fixed) values of lambda_s (l_s), lambda_l
% (l_l)
% init guess is the initial profile phi for fsolve
global D ksi

% fsolve for root of equations () specified in function diff_opp
fun = @(phi) diff_opp(phi, l_l, l_s, N, s);
phi_sol = fsolve(fun, init_guess);

% computes derivatives using first and last row of diff. matrices
phi_sol = [s.phir; phi_sol; s.phil];
ders = [D(1,:)*phi_sol; D(N+2,:)*phi_sol];

% compute differences corresponding to eqns
ders_diff = [];
ders_diff(1) = ders(1)-(l_s-l_l+s.phi0*l_l)*(l_l-l_s)/ (s.K(s.phir)*s.Sigmap(s.phir));
ders_diff(2) = ders(2)+l_l*s.phi0*(l_l-l_s)*(1-s.phil)/ (s.phil*s.K(s.phil)*s.Sigmap(s.phil));
end

%%%%%%%%%%%%%%%%%%%%%%%%%%%%%%%%%%%%%%%%%%%%%%%%%%%%%%%%%%%%%%%%%%%%%%%%%%%%%%%
function f = diff_opp(phi, l_l, l_s, N, s)
% given vector of function values phi, parameters l_s, l_l, number of grid
% points N and problem settings s, computes the value given by () to be
% found root of
global D ksi

phif = [s.phir; phi; s.phil];   % adding boundary values
a=1/2*(l_l-l_s);
b=-1/2*(l_l-l_s)+s.phi0*l_l;
c=1/(l_l-l_s);
dphi = D*phif;                  % numerical derivative of vector phi
dphi2 = dphi.*dphi;             % derivative squared

int = a*ksi.*dphi + b*dphi - c*D*(phif.*s.K(phif).*s.Sigmap(phif).*dphi);
f=int(2:N+1);   % omit boundary values for the problem to be square
end

%%%%%%%%%%%%%%%%%%%%%%%%%%%%%%%%%%%%%%%%%%%%%%%%%%%%%%%%%%%%%%%%%%%%%%%%%%%%%%%
function [D,x] = cheb(N)
% Trefethens construction of differentiation matrix
if N==0, D=0; x=1; return, end
x = cos(pi*(0:N)/N)';
c = [2; ones(N-1,1); 2].*(-1).^(0:N)';
X = repmat(x,1,N+1);
dX = X-X';
D = (c*(1./c)')./(dX+(eye(N+1)));     % off-diagonal entries
D = D - diag(sum(D'));                % diagonal entries
end
```

```
%%%%%%%%%%%%%%%%%%%%%%%%%%%%%%%%%%%%%%%%%%%%%%%%%%%%%%%%%%%%%%%%%%%%%%%%%%%%
function [D,x] = fd(N)
% construction of finite difference matrix
if N==0, D=0; x=1; return, end
x = linspace(-1,1,N+1)';
D = sparse(N+1, N+1);
B = [-1/2*ones(N+1,1), zeros(N+1,1),1/2* ones(N+1,1)];
D = spdiags(B, -1:1, N+1, N+1);
D(1,1:3) = [-3/2, 2, -1/2];
D(end, (end-2):end) = [1/2, -2, 3/2];
D = N/2*D;                          % h=2/N, 1/h=N/2
end
```

Listing 2: MATLAB source code for the steady state

```
%%%%%%%%%%%%%%%%%%%%%%%%%%%%%%%%%%%%%%%%%%%%%%%%%%%%%%%%%%%%%%%%%%%%%%%%%%%%%%%
function out = SteadyState(s, N, approach)
% computes the steady-state solution given by eqns (3.3)-(3.7) rescaled to
% [-1,1]

% values with no computation needed
phisinf = s.phir;
hlinf = -s.pcs;
% compute the value at h_l
F = @(phi) s.rho*s.phi0*hlinf-s.Sigma(phi);
philinf = fsolve(F, s.phir);
% solid front position
underint = @(phi) s.Sigmap(phi)./phi;
int = integral(underint, phisinf, philinf);
hsinf = hlinf - int/s.rho;
% computing full profile phi_steady rescaled to [-1,1]
odefun= @(t, y) s.rho*(hlinf-hsinf)*y/(2*s.Sigmap(y));
sol = ode45(odefun, [-1, 1], s.phir);
% construct grid
switch approach
    case 'cheb'
        x = cos(pi*(0:N)/N)';
        x = wrev(x);
    case 'fd'
        x = linspace(-1,1,N+1)';
    otherwise
        disp('wrong approach chosen')
end
% evaluate  solution on grid
phi_inf = deval(sol, x)';
% output structure
out =  struct('h_s', hsinf, 'h_l', hlinf, 'phi_s', phisinf, 'phi_l', philinf, 'phi', phi_inf, 'grid', x);
% if rho==0 => individual approach
if s.rho == 0
    hsinf = -s.pcs/s.phir*(s.phir-s.phi0);
    philinf = s.phir;
    phi_inf = s.phir*ones(size(x));
    out =  struct('h_s', hsinf, 'h_l', hlinf, 'phi_s', phisinf, 'phi_l', philinf,'phi', phi_inf, 'grid', x);
end
end
```

Listing 3: MATLAB source code for the nonzero-gravity problem

```
%%%%%%%%%%%%%%%%%%%%%%%%%%%%%%%%%%%%%%%%%%%%%%%%%%%%%%%%%%%%%%%%%%%%%%%%%%%%%%%
function sol = TimeDependent(s, N, t0, tfin, approach, lambda_init, phi_init)
% solves system of ODEs given by equations ()-()
% t0...initial time for zero gravity profile to be used
% tfin...final time for numerical integration
% lambda_init, phi_init optional, SelfSimilar deals with it accordingly

% pseudespectral OR finite difference approach, see fcns cheb and fd
global D ksi                    % differentiation matrix, nodes as global
switch approach
    case 'cheb'
        [D,ksi] = cheb(N+1);    % N+2 - length incl. boundary values
        ksi = wrev(ksi);        % revert order of cheb. nodes for clarity
        D = -D;                 % revert diff. matrix for the same reason
    case 'fd'
        [D,ksi] = fd(N+1);
    otherwise
        disp('wrong method chosen')
        return
end

% construct initial value for system of ODEs from zero gravity case
switch nargin
    case 5
        sol_init = SelfSimilar(s, N, approach);
    case 6
        sol_init = SelfSimilar(s, N, approach, lambda_init);
    case 7
        sol_init = SelfSimilar(s, N, approach, lambda_init, phi_init);
    otherwise
        disp('Incorrect number of input arguments to the function TimeDependent')
end
h_s = 2*sol_init.lambda_s*sqrt(t0);     % initial front position
h_l = 2*sol_init.lambda_l*sqrt(t0);     % initial front position
v0 = [sol_init.phi(2:N+2);h_s;h_l];     % resulting initial values: first value corresponding to constant phir
                                        % omitted; h_s, h_l added

% use built-in solver for stiff systems of ODEs ode23s
odefun = @(t,v) ODEfun(t,v,N,s);        % anonymous function to be passed to solver
[t,y] = ode23s(odefun, [t0,tfin], v0);

% construct output structure
phi = [s.phir*ones(length(t),1), y(:,1:N+1)];   % add BV phir at all times
sol = struct('phi', phi, 'h_l', y(:, N+3), 'h_s', y(:, N+2), 't', t, 'grid', ksi, 'init', sol_init);
end

%%%%%%%%%%%%%%%%%%%%%%%%%%%%%%%%%%%%%%%%%%%%%%%%%%%%%%%%%%%%%%%%%%%%%%%%%%%%%%%
function [ w ] = ODEfun(t, v, N, s)
% system of ordinary differential equations given by ()
global D ksi

phi = [s.phir; v(1:N+1)];   % full profile phi
psi = v(N+1);               % extract time dependent BV psi
h_s = v(N+2);               % extract solid fornt position
h_l = v(N+3);               % extract liquid front position

jedn = ones(N+2,1);         % vector of ones
dphi = D*phi;               % vector of first spatial derivatives
dphip1 = dphi(N+2);         % spatial derivative at 1
dphin1 = dphi(1);           % spatial derivative at -1

% approximate time derivative of phi, hs, hl, psi
c = -(1-s.phi0)/s.phi0*(psi*s.K(psi)/(1-psi)*(s.Sigmap(psi)*2*dphip1/ (h_l-h_s)-s.rho*psi));
```

```
dhs = c + s.K(s.phir).*(s.Sigmap(s.phir).*2.*dphin1./ (h_l-h_s)-s.rho.*s.phir);
dhl = c - psi.*s.K(psi)./(1-psi).*(s.Sigmap(psi).*2.*dphip1./ (h_l-h_s)-s.rho.*psi);
phiop = -((ksi-jedn)./(h_l-h_s).*dhs-(ksi+jedn)./(h_l-h_s).*dhl).*dphi - 2.*c./(h_l-h_s).*dphi - 2./(h_l-h_s).*D*(phi.*s.K(phi)....
      .*(s.Sigmap(phi).*2./(h_l-h_s).*dphi-s.rho.*phi));
dpsi = 1./s.Sigmap(psi).*( dhl.*(1+s.rho)-s.rho.*c );

phiop = phiop(2:N+1);           % exclude constant BV phir

w = [phiop; dpsi; dhs; dhl];    % bind together as output
end

%%%%%%%%%%%%%%%%%%%%%%%%%%%%%%%%%%%%%%%%%%%%%%%%%%%%%%%%%%%%%%%%%%%%%%%%%%%%%%%
function [D,x] = cheb(N)
% Trefethens construction of differentiation matrix
if N==0, D=0; x=1; return, end
x = cos(pi.*(0:N)/N)';
c = [2; ones(N-1,1); 2].*(-1).^(0:N)';
X = repmat(x,1,N+1);
dX = X-X';
D = (c.*(1./c)')./(dX+(eye(N+1)));   % off-diagonal entries
D = D - diag(sum(D'));               % diagonal entries
end

%%%%%%%%%%%%%%%%%%%%%%%%%%%%%%%%%%%%%%%%%%%%%%%%%%%%%%%%%%%%%%%%%%%%%%%%%%%%%%%
function [D,x] = fd(N)
% construction of finite difference matrix
if N==0, D=0; x=1; return, end
x = linspace(-1,1,N+1)';
D = sparse(N+1, N+1);
B = [-1/2*ones(N+1,1), zeros(N+1,1),1/2* ones(N+1,1)];
D = spdiags(B, -1:1, N+1, N+1);
D(1,1:3) = [-3/2, 2, -1/2];
D(end, (end-2):end) = [1/2, -2, 3/2];
D = N/2.*D;                          % h=2/N, 1/h=N/2
end
```